Gas flow visualisation in low aspect ratio packed beds by three-dimensional modelling and near-infrared tomography

Faris Alzahrani[1], Mohammed Aldehani[1], Hao Rusi[2], Michael McMaster[2], Daniel Luis Abreu Fernandes[3], Suttichai Assabumrungrat[4], Meabh Nic An tSaoir[2] and Farid Aiouache[1*]

1. Department of Engineering, Lancaster University, UK
2. School of Chemistry and Chemical Engineering, Queen's University Belfast, UK
3. Department of Chemistry - Ångström Laboratory, Uppsala University, Sweden
4. Centre of Excellence in Catalysis and Catalytic Reaction Engineering, Department of Chemical Engineering, Chulalongkorn University, Thailand

*Corresponding author
E-mail: f.aiouache@lancaster.ac.uk

ABSTRACT

Non-uniform local flow inside randomly porous media of gas-solid packed beds of low aspect ratios ranging from 1.5 to 5 was investigated by three-dimensional modelling and near-infrared tomography. These beds are known to demonstrate heterogeneous mixing and uneven distributions of mass and heat. The effects of the confining wall on flow dynamics were found nonlinear, particularly for aspect ratios lower than 3. High velocities were mainly observed in regions near the wall of aspect ratio value of 1.5 and those of values higher than 3, owing to high local porosities in these zones. Mass dispersion characterised by both experimental near-infrared imaging and by particle tracking showed discrepancies with literature models, particularly for aspect ratios lower than 3. Uncertainties were more significant with the radial dispersion due bed size limits. Beyond this value, the wall affected more the axial dispersion, confirming the nonlinear impact of the wall on global hydrodynamics.

1. INTRODUCTION

Packed beds of low aspect ratios (ARs) of tube to particle diameters are commonly used in various industrial applications, owing to their simple arrangement and high surface-area-to-volume ratios, leading to integrated heat and mass exchanges. Driven by reduced pressure drops and improved heat exchange, innovative designs of these low AR packed beds have been demonstrated for applications including catalytic reactors (i.e. steam reforming, composite structured packing, nuclear reactors, meso- and micro-chemical reactors) [1-5], separators (i.e. dehumidification adsorbers for energy storage [6], chromatographic columns, filters and CO_2 sequestration) and thermal exchangers (compact heat exchangers). These growing applications have attracted interest into understanding local phenomena taking place using both advanced experimental tools and advanced modelling. Unfortunately, these tools were not sufficiently dedicated towards very low AR packed beds (i.e. AR less than 5) owing to disperse phenomena taking place, requiring spatially resolved observations. This applies even more to gas flow dynamics where phenomena of mixing and dispersions are strongly affected by density and temperature changes.

Although limited by the confining walls, models of fluid flow in these packed beds have been historically based on simplified one-dimensional (1D) pseudo-homogenous models or heterogeneous

two-phase models. Improvements of these models contained introduction of the two-dimensional (2D) models with inclusion of concepts of axial or longitudinal dispersion and radial or transversal dispersion, relying on the average structure of porosity. The 2D models of heat and mass configurations rely on lumping the local structure and the local flow velocity inside the packing and between the packing and the containing wall, and whose key parameters (i.e. porosity, permeability, viscosity and dispersion constants) are estimated by experimental data and regression analysis of appropriate models.[7] These 1D and 2D models are as well driven by empirical solutions, yielding to disagreements between the data of various literature works obtained inside the packing as well as those in regions in the vicinity of the confining walls, and thus rational understanding of crucial underlying phenomena is still challenging. [1-4] Furthermore, these models raise issues of arbitrary combinations of the non-Darcy (grain) and the non-porous Darcy scales and provide challenging representations of the non-slip/slip assumptions or actual viscosity at the surface of the grain[8]. This is particularly the case of low AR packing, where the tube wall affects and the local phenomena strongly dominate.[2-4, 9] Owing to the limitation in space resolution of the detailed flow picture inside these beds, these models yield to low insights into the local mechanisms and possible methods of controlling the rates of chemical or transport events.[10] In reality, thermal energy is transported by radial convective flows as fluid is displaced around the packing elements, while features of the flow in regions of stagnant and reverse exits have been identified by a number of spatially resolved experiments.[11-13] Local insights are known to be linked to performances of flow dynamics as well as heat and mass transfers, leading to requirements of more realistic levels of knowledge of transport processes by three-dimensional (3D) modelling.

The 3D modelling of the flow field and transport using actual or computer-generated bed shapes has been growing through the last few years as it offers comparable spatiotemporal resolution with 3D experimental methods such as tomographic techniques (i.e. X-ray computer tomography, magnetic resonance imaging (MRI), laser Doppler anemometry, etc.)[2, 3]. From the 3D simulation results, profiles of radial porosity, velocity, temperature, and dispersion are becoming accessible from a sufficient amount of data, while a limited number of experiments are used. Laboratory experiments on local velocity profiles were visualised for liquid flow by Giese et al.[10] using the refractive index matching technique and by Gladden et al.[14] using MRI, ascertaining many simulation works on fluid flow in porous media of different structures (spheres, cylinders, ordered, disordered, monodisperse and polydisperse, and so on).

The approaches using 3D modelling, are still however limited by requirements of large memories and computational power.[3] Current simulations, consisting of hundreds to over a thousand packed particles, still require large computation time, leading to simulations being carried out for small or laboratory scales [1, 15] . An alternative option to take into account actual or local structures of packed beds is to couple the fluid flow with the radial variation of porosity.[9] Radial distribution of porosity is a structural characteristic of packed beds and presents a significant importance for beds with low ARs of tube-to-particle diameters owing to the influence of the confining wall. The spheres near these walls form more ordered structures than spheres in the internal regions, leading to oscillatory trends of porosity and to damping behaviours in the near-wall regions. This damping profile has been demonstrated by Roblee et al.[16], who used cork spheres within molten wax, as well as by Sederman et al.[17], who used the MRI technique to observe the flow of water through a packing of ballotini spheres. The damping profile could be computed by combining the angularly averaged data from a limited number of cross-section projections of porosity and then expressed in terms of empirical, semi-empirical or analytical models.[18-22] Accuracies of these models were either good in regions near the wall or the centre of the packed bed but were rarely good for both regions. For instance, Mueller et al.[23, 24], who described the oscillations with a Bessel function of the first kind of order zero and the radial damping with an exponential function, developed a model that over-predicts the radial porosity near the wall but describes the radial porosity accurately when the radial distance increases from the

wall. Govindarao et al.[5] developed analytical expressions using concentric cylindrical channels of good accuracies in the near wall regions, particularly for packed beds of large AR. Dixon et al.[25] improved the semi-empirical models by computing the effect of the shape of beads (i.e. spheres, cylinders or hollow cylinders). Theuerkauf et al.[15] used the discrete element method (DEM), which accounts for particle-particle and particle-wall mechanical interactions to measure particle-scale structure and porosity in a series of beds with AR in the range 3-20.

The confining wall of low AR packed beds affects not only the porosity distribution but the fluid flow in terms of velocity and pressure drops as well. Early investigations by Kozney, [26] Carman and Ergun[27, 28] essentially used Darcy and Forchheimer approaches for randomly distributed particles. However, Happel, [29] Anderson, [30] Molerus, [31] and Eisfeld and Schnitzlein[32] used knowledge of the local flow behaviour near the solid surface inside the packing. The distribution of the local velocity in the inter-granular space, the pressure drop, and the permeability were found to be affected by the flow regime, the internal structure of the packed bed, the dimensions and the shapes of both the particles and the packed bed.[33] The flow behaviour was a function of interactions between the fluid, the particles and the column wall.[34] In addition to the flow, the confining walls have effects on the dispersion of species and heat in packed beds of low AR. Influenced by the structural porosity of the packing, the interaction of convective and diffusive transport presents trends of residence time distribution and dispersions of different trends than those observed in large AR packed beds.[2] The mass dispersion of species inside 3D-packed beds are recurrently validated by means of the averaged radial component (D_{rad}) and the averaged axial component (D_{ax}) of dispersion. These components are computed by mass dispersion experiments which use either a continuous approach of chemical concentration tracing or discontinuous approach of particle tracing to fit dispersion constants at dynamic operations. The later approach, which uses the DEM, is a Lagrangian method where movement of concentration equivalent particles are tracked instead of fluid species. The convective motion along streamlines and by a diffusive motion between different streamlines allow distribution of the particles to be reconstructed and the underlying models of axial and radial dispersions as a function of the dimensionless Peclet number (Pe) to be developed.[2]

These experimental works were mainly applied to liquid flow while those applied to local gas flow were rarely approached owing to insufficient maturity of relevant methods, leading to uncertainty on existing simulation results, particularly under non-isothermal flow and changes in density, viscosity, etc. Optical tomography, such as laser-based near-infrared (NIR) tomography, was demonstrated as promising technique to visualise fluid flow in packed beds of low scattering properties. Simultaneous measurements by absorption spectroscopy and two-line thermometry allowed 3D distributions of temperature and concentrations inside packed bed adsorbers and reactors to be visualised at spatial resolution of millimetres. Qualitative observations of NIR tomography results revealed uneven distributions of temperature and compositions caused by the flow maldistribution, channelling and intra-particle rate limitations. The major advantage of laser-based tomography to fluid flow inside packed beds with low aspect ratio (AR) is driven by the low scattering of the source intensity. The values of the number of scattering or optical depth (OD), as expressed in Appendix A1, is lower than unity for packed beds of ARs less than 10, suggesting a ballistic light propagation through the packing and allowing the modified Beer-Lambert law to be applied to local concentration measurements.[35]

In this work, 3D modelling and spatially resolved NIR tomography are used to visualize the fluid flow and spatial distributions of species in gas-solid packed beds of randomly distributed particles, subject to wall effects. The approach is extended to packed beds of ARs ranging from 1.5 to 5 and flow regime ranging from laminar to transitional flow limits (Re ~400). The results of experimental tests are used to validate 3D computer fluid dynamics (CFD) modelling. Knowledge of fluid flow in low AR packed bed is still scarce, particularly for AR less than 3, where packed beds show more local heterogeneity, less fluid mixing and uneven structural porosity, making fluid flow and

dispersion profiles unexpected. We explore the effects of the confining wall under the knowledge of flow dynamics (i.e. local structure of the packed bed, pressure drop and interstitial flow in the void space) by 3D CFD modelling and the results are validated by those obtained by global pressure drops and spatially resolved NIR imaging and literature models. In order to ease the computation requirements of 3D modelling, the results are subsequently compared with those obtained by 2D modelling, where structural porosity maps were obtained from actual 3D porosity distributions. The work plan includes the following steps: (1) transient changes of water vapour H_2O_v in D_2O vapour by NIR tomography is briefly described; (2) generation by DEM of representative bed geometries and comparison of the bed structure property, such as average porosity and spatial distribution of porosity with literature models; (3) observation of pressure drops and local velocity distributions and comparison with 3D modelling as well as relevant 2D literature models; and (4) observation of mass dispersion by NIR tomography and DEM modelling and comparison with those obtained by 2D modelling and literature models.

2. EXPERIMENTAL SECTION

2.1. Near-infrared imaging tomography tests

The experimental setup and procedure are detailed in our previous works[12, 35]. Briefly, the packed bed tube was made of fused quartz (12 mm internal diameter (I.D.) and 39 mm length) and was filled with hydrophobic quartz glass beads as shown in Figure 1 (a_1). the beads were made hydrophobic by surface cleaning in acid solution, methylisation using a film solution of methyl-trichlorosilane in toluene and washing with a solution of ethanol/water.[36] The tomography technique relied on 2D projected images from parallel scanning, where a NIR laser source (Santec TSL-510 with a modulating range from 1340 to1440 nm) and a NIR detector (Mosir 950 detector, 1024 x 256 pixels, 26 x 26 μm^2/pixel) were rotated linearly by a servo-motor to acquire transmitted projections through the packing medium. The laser beam was tuned to the high-absorption frequencies of water vapour H_2O_v, polarised before being collimated by a series of mirrors and cylindrical lenses in order to shape a top-hat and rectangular sheet beam of 12.0 x 39.0 mm^2 size as shown in Figure 1 (a_2). The tomographic reconstruction was performed by running a Matlab code based on the adaptive algebraic reconstruction technique, where the reconstructed 3D domain array of discrete voxels of absorbance or concentrations was solved by the Kaczmarz method.

Typically, water vapour was introduced to the system from a controlled evaporator mixer (Bronkhorst) at a flow rate of 0.1 to 0.5 $cm^3\ min^{-1}$ of N_2, a water composition of 6.0 mol. % (relative humidity of 30.5%) and temperature of 333 K, with all pre- and post-packed tube pipes being insulated and heated to the operating temperature. In addition, a humidity sensor (Exo Terra Digital Hygrometer, accuracy 2% at relative humidity > 10%) was placed at the exit of the experimental setup. The water vapour was introduced to the system and was allowed to stabilize for a period of hours to reach packing saturated before the commencement of an experiment by switching to deuterated water vapour D_2O_v. The outlet products were validated by quadruple mass spectrometer. To prevent any inference from moisture in the surrounds of the experiment the entire setup was enclosed in a black-shielded Perspex box. The extinction coefficients of H_2O_v across the packing section was obtained by using a squared quartz cell of 10 x 10 mm^2 cross-section and 100 mm height, which was half-filled with the quartz beads. The laser source was modulated to absorption lines of H_2O_v at 1380.685 nm as shown in Figure 1(b) and the spectrum above the packing (free of scattering) was validated with deviation in the transmittance of 0.4 mol.% for H_2O_v.

2.2. Pressure drop tests

Since literature data of fluid flow for low ARs are limited, experimental tests of pressure drops for ARs ranging from 1.5 to 5 were carried out by using a range of ARs. Air was used as a flowing gas

and the flow rate was controlled by a mass flow controller (ROD-4A, Advanced Energy). The pressure drops over the bed were measured free of pressure loss at the distributor with a differential pressure transducer (142PC02D, Sensortechnics GmbH), as shown in Figure 2 (a).

2.3. 3D flow modelling

2.3.1. Packing generation by DEM

A granular packing of densely spherical particles was built by means of DEM in order to mimic experimental samples. The 3D DEM code was written in the built-in FISH programming language of particle flow code 3D (PFC^{3D}) and was used to generate realistic packing samples of random structures with ARs ranging from 1.5 to 5, as shown in Figure 2 (b). The structure of the packing was the function of properties of both the container and the particles, including the stiffness, the density, and the friction coefficients between the particles or the particles and the confining wall. The compaction process was carried out until the maximum unbalanced contact force between particles reached a value of the order 10^{-7} N, resulting in a packing at static equilibrium. The stiffness coefficients of the wall and the particles were varied for maximum density of the packing. The overall setting parameters have been enlisted in Table 1. The packing geometry, which was defined by the 3D coordinates of particle centres, was then embedded into the commercial CFD package COMSOL Multiphysics 4.4 via 3D AutoCAD (Autodesk) processing, allowing a dedicated meshing to take place by using a computer with 128 GB RAM.

2.3.2. Fluid flow model

The model of a laminar gas flow in a 3D porous media is governed by both the mass conservation (equation (1)) and the Navier-Stokes momentum equation (equation (2)), where the inertial forces includes both the pressure forces and viscous forces (the stress-strain tensor for a Newtonian fluid).

$$\rho \nabla . u = 0 \qquad (1)$$

$$\rho(u.\nabla u) = -\nabla p I + \nabla.\left(\mu(\nabla u + (\nabla u)^T - \frac{2}{3}\mu(\nabla . u)I\right) \qquad (2)$$

The inlet boundary was a fixed velocity inlet condition; this was spatially uniform over the inlet (equation (2.1). At the outlet, a constant atmospheric pressure (p_0) boundary condition (equation (2.2.)) was used. In addition, no slip conditions were assumed at wall-fluid and particle-fluid interphases.

$$u = -u_{in}\mathrm{n} = 0 \qquad (2.1)$$

$$p = p_0,\ \left(\mu(\nabla u + (\nabla u)^T - \frac{2}{3}\mu(\nabla . u)I\right)\mathrm{n} = 0 \qquad (2.2)$$

In these equations, μ is the fluid molecular viscosity and ρ is the fluid mass density.

The stationary solver of Comsol package with default setting was used. The governing equations (1) and (2) were solved using the finite volume approach. The domain of interest between the solid particles was divided into numerous cells where the governing equations were integrated across the volume of each cell. The integrals converted the governing equations into a set of difference equations which were solved numerically using the generalized minimal residual method (GMRES) with the Geometric Multigrid pre-conditioner. The GMRES algorithm is an iterative method for the numerical solution of a non-symmetric system of linear equations. The method approximates the solution by the vector in a Krylov subspace with minimal residual. Trial studies with a variety of solvers (FGMRES,

conjugate gradient, BiCgStab) indicated that in these particular cases, the simulation result was fairly insensitive to the exact one. The convergence was evaluated based on relative tolerance which was set to 0.0001.

The discretisation was carried out by the built-in meshing module of Comsol using the Adaptative Mesh Refinement Method which generated predominantly tetrahedral domain elements and triangular surfaces. The effects of the size of these elements on the viscous forces, particularly in area where potential skewed meshes could be generated such as particle contact points were investigated. This was insured by a mesh convergence check for each packed bed by increasing the number of mesh elements and monitoring the pressure values at three arbitrary locations from the CFD simulation. It was observed that the packed beds of high AR required refined meshing than the low AR to reach approximately stable values of pressure. This result was subsequently confirmed by using the Grid Convergence Index (GCI) as described in Appendix A2.[37] The GCI reached values below 2 %, validating the reasons to trust the accuracy of the present numerical simulations and to ensure that the solution is independent of the mesh size.

In addition, the quality of the mesh was analysed by the minimum element quality statistics method which expresses the contribution of the skewed elements. The spherical particles in the packed bed were expected to release skewed elements which were extensively reported in literature. These dealt with such elements by increase or the decrease of particle sizes as well as using the range of features available in commercial CFD to smooth these skewed elements. Herein, the diameter size of particles was reduced by 1% in all our tests. Such shrinkage was found necessary to prevent highly-skewed meshes at single-point contacts between particles while maintaining reasonable computation time.[2, 23-25] A shrinkage higher than this value would yield no advantage in producing more accurate results and would be computationally more expensive.

2.3. 3. Mass dispersion model

Dispersion of species in porous media is generally characterised by five regimes; pure molecular diffusion regime (Pe<0.3), superposition regime (0.3<Pe< 5) where the effect of molecular diffusion and dispersion are comparable, predominant mechanical dispersion regime (5<Pe<300), pure mechanical dispersion regime (300<Pe<100000) where the effect of molecular diffusion is negligible and dispersion out of Darcy domain regime (Pe> 100000) where the effects of inertia and turbulence cannot be neglected.[38] The dispersion in a packed bed is well described by the two-dimensional diffusive and convective model equation, assuming constant velocity u and constant dispersion coefficients.

$$\frac{\partial C}{\partial t} = D_{ax}\frac{\partial^2 C}{\partial z 2} + \frac{1}{r}\frac{\partial}{\partial r}\left(D_{rad} r \frac{\partial C}{\partial r}\right) - u\frac{\partial C}{\partial z} \qquad (3)$$

The analytical solutions, by assuming a maximum concentration at the centre of the packed bed, as expressed by equations 4 and 5, require continuous species tracing under steady-state transversal and dynamic radial mass dispersion experiments.

$$\frac{C(r,z)}{C_o} = \frac{1}{2} erfc\left(\frac{r}{2\sqrt{zD_{rad}/u}}\right) \qquad (4)$$

$$\frac{C(t,z)}{C_o} = \frac{1}{2} erfc\left(\frac{z-ut}{2\sqrt{D_{ax}t}}\right) + \frac{1}{2}\exp\left(\frac{uz}{D_{ax}}\right) erfc\left(\frac{z+ut}{2\sqrt{D_{ax}t}}\right) \qquad (5)$$

Where C_0 is the inlet concentration. An alternative discontinuous approach relies on the Lagrangian method by following distinct particles along a trajectory in a steady-state velocity field. The method of moments, as shown in equation (3), is used to calculate axial and radial dispersion coefficients.[1]

$$D_{ax/rad} = \frac{1}{2}\frac{d\sigma^2_{ax/rad}}{dt} \quad (6)$$

Here, $\sigma_{ax/rad}$ is the second moment or mean square deviation, as defined by equations (7) and (8):

$$\sigma^2_{ax}(t) = \frac{1}{NP}\sum_{n=1}^{NP}(x_n(t) - \bar{x}(t))^2 \quad (7)$$

$$\sigma^2_{rad}(t) = \frac{1}{NP}\sum_{n=1}^{NP}(r_n(t) - \bar{r}(t))^2 \quad (8)$$

Here, *n* is the particle index, *NP* is the total number of tracked particles, *x* and *r* are displacements of particles along the axial and radial coordinates, respectively. $\bar{x}$ and $\bar{r}$ are the averaged displacements of all particles along the axial and radial coordinates, respectively.

3. RESULTS AND DISCUSSION

3.1. Fluid flow profiles by 3D modelling

3.1.1. Structural porosity profiles

It should be noted that the trends of packed bed porosity have been generally analysed by two methods. The first, which was followed by early studies, relied on experimental data of packing structures and where much attention was paid to the wall effects and periodic variation of porosity away from the containing wall.[39,40] The second used computer-generated packing through a variety of computational algorithms. [40,41] Both computer-generated[42] or hand-built packing[43] relied on models which use a two-point correlation function of sphere centres and the tessellation of the void space distribution of the inter-particle interstices using a number of schemes, such as tetrahedral,[44, 45] Dirichlet[46] or Voronoi types.[47, 48] Although the tessellation permitted some statistical description of pores and interstices, it was unable to give a complete analysis which relies on the overall geometry of the individual pores. In contrast, direct analysis of the void space itself is possible via image analysis techniques, which take as input the 3D tomographic or 3D visualisation data.[49] Compared with 2D images, the 3D visualisation of the pore space allowed access to 3D topology of the pore space (e.g. the connectivity of local elements) with similar resolution in each dimension. These structural characteristics determined the velocity, pressure drop, and mass transfer characteristics of the bed. Of course, the same information can be obtained by recording a succession of 2D slice sections for which the slice thickness is equal to or better than the in-slice resolution, and then reconstructing the 3D structure. It is the direct analysis via 3D visualisation data that was followed in this work.

The procedure used available data in the 3D matrix that defines coordinates of particles inside the packed bed. For instance, Figure 2 (b) illustrates generated packing arrangements for AR of 3 by experimental data and DEM. The porosity profiles of packed beds of different AR were calculated by using the data of various spatial domains, which were denoted as 'Domain Index (DI)' in COMSOL software. Domain index is a single integer number and was allocated to mesh boundaries of a single domain area (solid particle or between particles), allowing access to porosity distribution at any 3D coordinate with a spatial resolution at mesh size limits. Just like the distribution shown in Figure 3 (a), the cylinder container of the packed bed of 100 mm length was cut into 100 slices

allowing a spatial resolution along the axial direction of 1 mm. A sample of DI data accessible for a single slice is shown in Figure 3(b). It is interesting to see that the distribution of accessible DI data is not uniform as it follows mesh distribution (i.e. dense data at particle contact points). The exported data files were then processed for porosity distribution of the packed bed by developing a Matlab code for the procedure illustrated in Figure 3 (c). First, the domain index of the area between the particles was considered fully porous with an integer number of unity, and the remaining domain indexes that belong to solid particles were considered non-porous with an integer number of zero (step 1 in Figure 3(c)). The 3D DI data were angularly averaged into 2D data where angular weight of accessible DI data was taken into account (step 2 in Figure 3(c)). The released 2D data represent the surface fraction (ε_s) non-occupied by the solid particles if the packed bed was represented by a 2D configuration. The surface fraction ε_s was subsequently reduced into '1D' axially averaged porosity (step 3 in Figure 3(c)) and global or averaged porosity of the full packed bed (step 4 in Figure 3(c)).

Table 2 illustrates the porosity data obtained in the present simulation for various aspect ratios. A comparison with a model from Zou et al. [49] shows a good agreement, particularly for low AR. With the exception of AR of 2, the loose structure of generated packing by shrinking the particles by 1 % was well observed and it increased to a large AR. More insights into the loose structure have been shown in the 2D maps of the circumferentially averaged DI data in Figure 4. The loose structure along the axial coordinate is confirmed along the axial coordinate of the packed bed for various ARs. The surface fraction of empty space ε_s of a selected location of the packed bed could be larger or smaller than the entire corresponding bed, depending on where the location was selected and how many particles were included in the selected location.

Moreover, Figure 4 shows ε_s of the selected locations and how it deviated from the entire packed bed porosity in Table 2 when the numbers of particles in the segments varied. It is interesting to see the periodic variations of ε_s for all AR arrangements, corresponding to the layer changes in the packing. The deviations suffered from a jump every time additional particles constituted a new layer of packing and then decreased as more particles were added to the same layer. For high AR, the particle number further increased. The local porosity could be either larger or smaller than the entire bed, but the deviation was relatively small. The larger the AR was, the more particles were needed to reach this low-level deviation of packing porosity. This is because sufficient layers were required to represent the entire packed bed, and a packing with a larger AR contains more particles per layer. Such cyclic changes of the porosity of the height of the bed could be reflected by cyclic variations of interstitial flow velocity and mass dispersions.

Taking the axially averaged porosity for these figures, which represent the distribution of porosity along the radial coordinate within the packing system, was the next step to compare simulation results with the semi-analytical model of the radial porosity distribution by Mueller et al.[50] as shown in Figure 5. Similar oscillation trends with damping profiles towards the centre of the packed beds were observed. The discrepancies in regions towards the centre confirm the loose structure of the generated packing. On the other hand, the radial distribution of porosity obtained was in good agreement with the models of Mueller, especially close to the wall, while the porosity increased at low AR due to high porosity near the wall in packed beds. Such property distribution of porosity impacts the flow dynamics and mass transfer, as described in the following sections.

3.1.2. Pressure drop profiles

The pressure drops, in terms of dimensionless number *P*, in packed beds of ARs of 1.5 and 5 at flow regime up *Re* of 400 were compared with established models of Carman, Ergun, Zhavoronkov and Reichelt as shown in Figure 6 (see Appendix A3 for more details about the four models). The results

of pressure drops by CFD simulation fit the models predicted by Zhavoronkov, Reichelt and Ergun well at high Reynolds numbers, but showed disagreements with the Carman model, which is suitable for packed beds of large AR.

The pressure drops are as well represented in terms of pressure drops ratios, P/P_{inf}, in order to account for the effect of the wall for low AR values. P_{inf} is the dimensionless pressure drop for an infinite AR. The simulation results as on the effect of AR of packed beds on pressure drops at laminar and transitional flows are shown in Figure 7 (a) and were validated using experimental data and literature models, as shown in Figures 7 (b_1-b_4), respectively. An increase of pressure drop ratios at low AR packed beds was observed at AR less than 3 while those obtained by Ergun and Carman models were not sensitive to AR values. The simulation results fit the Reichelt model better, and the decrease in the pressure drops at AR lower than 3 was interpreted by Eisfeld and Schnitzlein by two counteracting effects of the wall: one to offer additional resistance due to wall friction - this effect will be less at $Re > 200$ - and the other positive effect, which represents reducing the pressure drop with Reynolds number due to increased porosity in the vicinity of wall.[32]

In order to ascertain this important finding of the decrease of the wall effect at AR lower than 3, the fluid flow in a 2D porous media of packed map of circumferentially averaged porosity in Figure 4 was carried out (see Appendix A4). The porosity distribution map for the 2D model was obtained by interpolation with a spline function, allowing access to data which were not visualized by the 3D non-transparent arrangement. As expected, the results clearly showed more porosity distribution in the centre of the packed bed for even numbers of AR values (i.e. 2 and 4) and less porosity distribution for uneven numbers of AR (i.e. 3 and 5). Between consecutive even and odd numbers of AR, the trends were found however non-linear for AR less than 3s shown by AR of 2.5. For this value of AR, porosity distribution shifted toward than AR value of 2, allowing more flow in the centre of the packed bed than AR values of 2, 3 or 5. The wall effect and subsequent porosity distribution along the radial direction thus took place progressively as the porosity increased in the vicinity of the wall towards AR of 3, offering more selective channelling and by inference velocity in these regions. The wall effect decreased again for AR higher than 4, owing to more mixing in the centre of the packing. Thus, there is a non-linear wall effect, which is the exclusive function of fluid flow rate as shown in Figure 7.

3.1.3. Velocity field profiles

Since no symmetry exists in the unstructured packing, the flow structure is expected to be highly dependent on the topology of the inter-granular space at pore scale. Figure 8 shows the projections of local velocity on cross-sectional and vertical planes along the bed length at AR of 1.5. It is clear that interpreting a suitable visual output of velocity is a challenging task without a direct line of sight through the full packed bed. The disorder of the flow structure by 3D view however can reveal the presence of vortices and eddies in the pores, particularly at high velocity fields.

Alternative viewing option of the complex 3D domain is by a 2D angularly averaged domain as it offers more realistic full picture of flow behaviour, as shown in Figure 9 for ARs of 1.5, 2, 2.5 and 3. Such detailed analysis of flow structure would be relevant provided that the 2D porous structures in Figure 4 are as close as possible to the real 3D structures. Figure 9 (a) shows velocity distribution for AR of 1.5 mainly in the near-wall regions, demonstrating effect of wall. This effect slightly decreases for AR value of 2, as shown in Figure 9 (b), where some spots of velocity are displayed along with the continuous distributions near the wall regions. Increasing the value of AR to 2.5 promoted the spots of values into continuous values, which correspond to a more homogeneous velocity than those observed at an AR of 2, which in turn displays less homogeneous velocity than that at 3. This later packing however, shows less homogeneous velocity distributions than at AR of 5, yielding to expected trends of effect of the confining wall on fluid flows at low AR. Contrary to the magnitude

of velocity inside the packed bed of AR of 2, the magnitude of the spots along the tube wall for ARs of 3 and 5 are not sufficiently high, confirming the looseness of the packing in these regions.
These results are in agreement with experimental data reported by Aiouache et al., [12] where preferential channelling near the wall has been experimentally demonstrated. The fluid velocity was the greatest in the narrow spaces at ARs of 4 and 5 because it occurred in between particle-to-particle contacts and particle-to-wall contacts, where the flow was forced to accelerate through a relatively smaller space. Similar to porosity trends, cyclic variations of velocity along the bed height is again observed, confirming local variations of fluid flow in low AR, particularly those of less than 3. This caused several areas of local maximum velocity where the fluid sometimes found its way into the channels. The 2D modelling approach was ascertained by comparing the results of pressure drops with those obtained by 3D modelling as shown in Figure 10. A deviation of 0.5% is observed for *Re* of 284, confirming the benefit of using porosity distribution from 3D maps to access insights into industrial packed beds of large computation time and hardware power.

3.2. Mass dispersion profiles

3.2.1. By spatially resolved NIR imaging

The measurements of light extinction across the packing were performed by using a squared quartz cell. Owing to the combination of absorption and scattering occurring in the packing bed, the spectra retrieved were of a higher transmittance than those retrieved from the gas phase above the packing as mentioned in section 2.1. The packing section, in absence of H_2O_v, exhibited an optical depth of 0.25 for a packed bed of AR of 4, suggesting relevance of a straight light propagation, with little scattering, and validating the use of the modified Beer-Lambert law for concentration measurements[35]. Furthermore, the tests of validation of the NIR imaging were carried out by using similar procedure employed in previous works[36]. First saturating the packed column with H_2O_v and the inlet flow of the inner tube of 5 mm I.D., as shown in Figure 1(c), was then switched to D_2O_v to begin the experiment. Both inner and outer flows were at a similar velocity. 3D reconstructed images of H_2O_v composition were generated at steady-state conditions for the projections taken at fixed angle steps of 15^o (thirteen projections/cycle) and lasted approximately 18 s. The maximum size of the pixel array of NIR detector that could collect the trans-illuminated NIR beam (size of 12.0 x 39.0 mm^2) was 80 x 700 pixels, leading to a spatial resolution of 0.15 x 0.056 mm^2.
The reconstruction images of the H_2O_v composition, after the introduction of D_2O_v at 0.1 m s^{-1} (Figures 11(a) and (b)) show vertical section and five cross-sections of composition maps, respectively. A decrease in the composition of H_2O_v with time is well displayed in the centre (inner flow) and a clear limit between the H_2O_v flow region (outer flow) and D_2O_v flow region (inner flow) is well discernible in the bottom slice at a spatial resolution of submillimetre. Although a dispersion of the two flows was not expected owing to high flow rates used, the inner (D_2O_v) and outer (H_2O_v) flows displayed some spots and increased mixing at section of the packing at averaged deviations with those obtained from mass spectrometer of 8.1 % for concentrations as low as 1.0 mol. % of water vapour. The higher accuracy of quartz bed compared to styrene di-vinyl benzene sulphonate resin packing used in previous work[35] is likely due to higher optical properties of the hydrophobic quartz beds.
These validation tests were then extended to tests for radial and axial dispersion measurements which were run through an isotopic exchange chemistry between H_2O_v and D_2O_v. A single AR of 4 was used owing to design limits of the field of view limits (39 mm) of the NIR imaging whilst a minimum length of the packing to particle ratio of 12 was required to avoid length effects [35].

3.2.1.1. Radial dispersion tests

The tests for radial dispersion were carried out using similar procedure of phantom tests but a much lower flow velocity was used (i.e. 0.00002 to 0.00011 ms^{-1}). The reconstruction images of the H_2O_v

composition, after the introduction of D_2O_v m s^{-1} (Figures 12(a_1) and (a_2)) show composition maps of five cross-sections and two vertical sections, respectively. A high composition of H_2O_v is well displayed in the vicinity of the wall (outer flow) but clear limits between the H_2O_v flow region and non H_2O_v -flow region are not easily discernible from the bottom slice (the exit of the inner tube) to the top slice (the end of the packed bed). Full 700 cross-sectional layers from the bottom to the top of the packed bed were gathered in a movie at a frame rate of 24 layers s^{-1} as shown in the supplementary material (S_1).

In addition, the 3D data, once 2D angularly averaged as shown in Figure 12(c_1), show clear distinction H_2O_v and non- H_2O_v regions, which extends radially from the bottom to the top of the packed bed. A comparison with the results from the mass spectrometer at the exit of the packing indicated relative deviations in H_2O_v composition of 9.1 %. These results are satisfactory given inherent errors associated with the experimental design (acquisition time per tomography cycle, light diffusion through packing, diffraction by the packing tube, convenient signal to noise ratio and both entrance and exit effects).[35]

3.2.1.2. Axial dispersion tests

The experimental procedure for axial dispersion tests were similar to those for the radial dispersion but were carried out under transient operations and the full inlet flow was switched to D_2O_v to begin the experiments. Figures 12(a_2) and (b_2) show the composition profiles of five cross-sectional and two vertical layers along the packed bed, respectively, which are representative of the breakthrough of D_2O_v after a spent time of 30 min. Full 700 cross-sectional layers from the bottom to the top of the packed bed were gathered in a movie at a frame rate of 24 layers s^{-1} as shown in the supplementary material (S_2). Axial dispersion might not be well observed through the composition changes of H_2O_v along the radial coordinates which reached values of 4.5 mol. %. A non-uniform distribution of composition is observed however in the packing which indicates that the local flow could be channelling between the glass beads. There is less mixing, and thus dispersion than in the bottom region, suggesting flow maps tend to be moving towards the centre of the tube. These results of the 3D distribution of compositions agree with previous velocity maps in section 3.1.3., the flow maldistribution in the vicinity of the wall where at the start the water vapour composition in the core remained smaller than the near-wall one. The 2D circumferentially (Figure 11 (c_2)) shows the effect of the wall on the flow maldistribution associated with the high composition of water vapour near the wall and a damped one towards the core of the packed bed. Such profiles correlates well with general trends of porosity profiles in Figure 4.

3.2.1.3. Discussions

The spatially resolved NIR imaging confirmed the non-uniform distribution of species in both tests and demonstrated potential access to local variations of both D_{rad} and D_{ax} along the radial and axial coordinates, owing to the cyclic changes of porosity, and by inference interstitial velocity, as demonstrated in previous sections. Local D_{rad} and D_{ax} could have been determined if the maps of H_2O_v were of higher spatiotemporal resolutions. The overall trends of D_{rad} and D_{ax} for the full packed bed as a function of flow profiles were therefore investigated and were obtained by fitting experimental data of H_2O_v by NIR tomography in section 3.2.1.1 and 3.2.1.2 to equations 4 and 5, respectively, and minimising the sum of squares of relevant residuals. Non-linear least squares algorithm based on the Marquardt method was then used to adjust the unknown dispersion constants. As to axial dispersion study, the 2D experimental maps were first circumferentially and radially averaged into 1D composition profiles along the bed height as shown in Figure 12 (d_2) and then fitted to the model of equation 5 to obtain unknown D_{ax} values. The model of equation 5 was also added to Figure 12 (d_2) which shows a good fit of experimental data with model. The slight deviation in the

regions close to the inlet might be caused by the effect of the inlet on the flow, which is known to be significant in laminar regimes. Average relative overall deviations were less than 9.1 % for all fluid flow values used. It is interesting then to see advantages of spatial imaging to reduce the number of tests for axial dispersion studies.
On the other hand, the radial dispersion study used the full 2D maps of H_2O_v obtained at steady-state conditions. The result of 2D fitting, along axial and radial coordinates along with equation 4 is shown in Figure 12 (d_1). Average deviations between the experimental data of H_2O_v and those obtained from the model (equation 4) were much important than the axial dispersion tests, ranging from 20 to 25 % for all tests.
The results of both D_{rad} and D_{ax} , normalised to molecular diffusion D_m, were validated by comparing their profiles along with the flow dynamics *Pe* to popular literature models (i.e. Freund[2] and Delgado[48]) as shown in Figure 13. It should be noted that these two models are not straightforward applicable for the low *Pe* numbers used. The results are broadly consistent with the range of dispersion coefficients obtained for *Pe* number under diffusion control where the D_m/D_{ax} approaches the tortuosity of the bed (i.e. a theoretical value of 1.4). Again, the prediction of axial dispersion is in good agreement with literature models while the radial dispersion showed some discrepancies, confirming again the good fit of NIR imaging for axial dispersion studies.

3.2.2. By DEM modelling

The results of mass dispersion uncertainties achieved by NIR tomography were validated by DEM. This later is a valid tool which has been extensively used for mass dispersion studies [1, 52]. It relied on Lagrangian particle tracking procedure where the distinctive motions of individual particles were added to describe their trajectories, and thus the macroscopic mixing of tracer particles along the axial and the radial directions of the packed beds. Herein, the particle tracking module of Comsol was coupled with the 3D fluid flow model (equations (1) and (2)) to give trajectories to individual particles of similar trends to those developed by the carrying fluid. The particles were assumed to be of negligible mass and subject to bounce conditions at the fluid-solid interphase. The design of the packed bed required addition of an inlet for particle flow by using a small cylinder of 1 mm I.D. and 2 mm height at the top centre of the packed bed. The size of the small cylinder was effective in terms of meshing requirements. About 500,000 particles were released for each test and the displacement of these particles was followed with time.

Interaction of AR and mass transport was investigated by using two values of AR (i.e. 2 and 4) and two values of *Pe* (0.01 and 100). Although the particles were released at the centre of the packed bed, their propagation at *Pe* of 100 along the axial direction was significant for both AR 2 and AR 4 and was dominant in comparison with the diffusive propagation along the radial direction, as shown in Figure 14. Significant holdups should be associated with zones where the fluid entered stagnant regions of reduced convective flow, leading to significant transport by diffusion. At *Pe* of 0.01, the particles however happened to collide at the solid/fluid interface, causing a significant diffusion along the radial direction. Compared with those observed in the vicinity of the wall at AR of 4, the particles were seen to circulate mainly along the centre of the packing at AR of 2, which agrees with the results of porosity and fluid flow. Beyond this value of AR, particles again circulated more in the central region of the packed bed. It should be noted that no particle was seen as trapped in stagnation zones, except at the interface fluid/solid. This means that if there were vortices inside which the current lines loop on themselves, they would be too small as number to be observed. Owing to the no-slip assumption, particles that reached the wall were eliminated for the computation of mass transfer dispersions.

Quantitative values of dispersion coefficients were then computed by accessing first to the trends of individual particle positions with time. These positions were used to compute trends of the second

moment or mean square deviation of positions of these particles along axial and radial directions according to equations (7) and (8), respectively. These values served to calculate the asymptotic values of dispersion coefficients according to equation 6. The profiles of axial and radial dispersion coefficients normalised to molecular diffusion were added to Figure 13, along with those computed by the semi-analytical models of Freund and Delgado[2, 51]. The prediction of axial dispersion is in good agreement with those obtained by NIR tomography in section 3.2.1 and literature models. Similar to NIR tomography, the radial dispersion by DEM showed some discrepancies with literature models, although for AR value of 1.5, there is some reasonable agreement with Freund's model. Similar trends were reported by Augier et al. [52] and the explanation could be given by the size of the packed bed, which was not large enough to allow asymptotic profiles of velocity to be reached by the particles. Axial dispersion values for a larger aspect ratio of packed bed (AR of 4) were between the models of Freund and Delgado. Unlike the radial dispersion, the axial dispersion was more promoted by the wall, confirming the impact of the wall on global mixing within low-AR packed beds, and suggesting that the DEM approach is a helpful tool to characterise such a phenomenon. Finally, the validated results from the 3D DEM were compared with those obtained from the 2D DEM, which used 2D angularly averaged porosity, as shown in Figures 14 (b_1) and (b_2). Unlike radial dispersion, axial dispersion by 2D modelling are in good agreement with those from 3D modelling, and thus validate the benefit of using 2D averaged maps of porosity for large-scale packed beds for mass dispersion studies.

4. CONCLUSIONS

In this work, gas/solid behaviour in narrow packed beds was investigated by 3D modelling and near-infrared tomography. Bed configurations of low ARs were generated and the structural porosity trends (3D, 2D and 1D) of randomly distributed particles subject to wall effects were compared with semi-analytical models. The results contributed to more understanding of fluid flow and mass transport in these low AR packed beds where knowledge is still scarce. The porosity profiles were in a good agreement with the semi-analytical models such as Mueller's expression, especially in the zone near the wall. Similar oscillation trends with damping profiles towards the centre of the packed beds were observed. The discrepancies in regions towards the centre may have originated from the loose structure of the generated packing. In addition, the average porosity obtained by the CFD simulation was in reasonable agreement with Zou's model, where the porosity increased at low AR. The simulation results were validated by a pressure drop and the results fitted well with Reichelt, Zhavoronkov and Ergun's models at high Reynolds numbers. Distribution of velocity was investigated and the results of high velocities were mainly observed in the regions near the confining wall of ARs of 3 and beyond, owing to high local porosities in these zones. Flow heterogeneity was also characterised by mass dispersion using both near-infrared imaging and DEM. Values of dispersions by both near-infrared tomography were consistent with those expected under diffusion control while some discrepancies for radial dispersion coefficients were observed due to the very short domain length, particularly for small values of AR. Unlike radial dispersion, axial dispersion showed agreements with DEM results and literature models. DEM has demonstrated that axial dispersion was promoted by the wall at AR of 3 and beyond, confirming the impact of the wall on global hydrodynamics inside low AR packed beds. Future works will extend use of NIR imaging to other applications species such as CO_2 storage in porous media and value of *Pe* to unity and beyond, where both diffusion and the advection take place, requiring however even more reduced data collection time, larger field of view and operating pressures.

ACKNOWLEDGMENTS

The authors would like to acknowledge the support for funding provided by the Department of Education and Learning (DEL), Saudi Arabia Government and Lancaster University starting grant and rat the Thailand Research Fund.

NOMENCLATURE

A_w Non-dimensional pressure drops model constant (-)

B_w Non-dimensional pressure drops model constant (-)

C Concentration (mol m^{-3})

D Tube diameter (m)

DI Domain index (-)

D_m Molecular diffusion coefficient (m^2 s^{-1})

d_p Particle diameter (m)

$D_{ax/rad}$ Axial or Radial dispersion coefficient (m^2 s^{-1})

e_a^{21} relative error (-)

F Drag force per unit of volume (N m^{-3})

K Permeability of the packed bed (m^2)

h grid size (-)

k Carman model constant (-)

m apparent order (-)

n' Carman model constant (-)

L length of bed (m)

n particle index

NP Number of Lagrangian tracer particles (-)

N Number of cells (-)

p *pressure drops (Pa)*

P Dimensionless pressure drop (-)

Pe Peclet number for mass dispersion (-)

r radial coordinate (m)

$\bar{r}$ Averaged displacements of all particles along the radial coordinates (m)

r_{21} *refinement factor (-)*

Re Reynolds number (-)

t Time (s)

P_{inf} Dimensionless pressure drop of an infinite size packed bed (-)

u Fluid flow velocity (m s^{-1})

u_s Fluid flow superficial velocity (m s^{-1})

x axial coordinate

$\bar{x}$ Averaged displacements of all particles along the axial coordinates

z Axial coordinate (m)

Greek letters

θ Angular coordinate (-)

Θ Pressure difference between two discretisations (-)

ρ Density (kg m^{-3})

ε Bed Porosity (-)

μ Dynamic viscosity (m^2 s^{-1})

η Fluid kinematic viscosity (m^2 s^{-1})

σ Standard deviation (-)

β Non-Darcy coefficient (m^{-1})

Δ V the cell volume

η Fluid kinematic viscosity (m^2 s^{-1})

Abbreviations

AR Aspect ratio

CFD *Computer fluid dynamics*

DEM Discrete element method

GCI Grid convergence index

GMRES Generalized minimal residual method

I.D. Internal diameter

MRI Magnetic resonance imaging

*NI*R near-infrared

OD optical depth

Pe Peclet number

v Vapour

Supporting materials:

S1: *Radial dispersion:* Movie at 24 frame/s for the Full 700 cross-sectional layers from the bottom to the top of the packed bed

S1.wmv

S2: *Axial dispersion at 12 min:* Movie at 24 frame/s for the Full 700 cross-sectional layers from the bottom to the top of the packed bed

S2.wmv

REFERENCES

(1) Freund, H.; Bauer, J.; Zeiser, T.; Emig, G. Detailed simulation of transport processes in fixed-beds. *Ind. Eng. Chem. Res*. **2005**, *44*, 6423-6434.

(2) Dixon, A.; Taskin, M.; Nijemeisland, M.; Stitt, E. CFD method to couple three-dimensional transport and reaction inside catalyst particles to the fixed bed flow field. *Ind.Eng. Chem.Res*. **2010**, *49*, 9012-9025.

(3) Vortmeyer, D.; Schuster, J. Evaluation of steady flow profiles in rectangular and circular packed beds by a variational method. *Chem. Eng. Sci.* **1983**, *38*, 1691-1699.

(4) Govindarao, V.M.H.; Subbanna, M.; Rao, A.V.S.; Ramrao, K.V.S. Voidage profile in packed beds by multi-channel model :effects ofcurvature of the channels. *Chem. Eng. Sci*. **1990**, *45*, 362-364.

(5) Dautzenberg, F.M.; Mukherjee, M. Process intensification using multifunctional reactors, *Chem. Eng. Sci.* **2000**, *56*, 251-267

(6) Pistocchini, L.; Silvia Garone, S.; Motta, M. Fluid Dynamics Optimization of a Novel Isothermal Adsorption Dehumidification System for Solar Driven Applications. *Energy Procedia* **2014**, *48*, 1689–1698

(7) Durlofsky, L.;Brady, J. F. Analysis of the Brinkman equation as a model for flow in porous media, *Physics of Fluids* **1987**, *30*, 3329-3341

(8) Jaree, A.; Hudgins, R.; Budman, H.; Silveston, P.; Yakhnin, V.; Menzinger, M. Hysteresis and extinction waves in catalytic CO oxidation caused by reactant concentration perturbations in a packed-bed reactor. *Ind. Eng. Chem. Res*. **2003**, *42*, 1662-1673.

(9) Zhang, W.; Thompson, K.; Reed, A.; Beenken, L. Relationship between packing structure and porosity in fixed beds of equilateral cylindrical particles. *Chem. Eng. Sci*. **2006**, *61*, 8060-8074.

(10) Giese, M.; Rottschafer, K.; Vortmeyer, D. Measured and modeled superficial flow profiles in packed beds with liquid flow. *AIChE J.* **1998**, *44*, 484-490.

(11) De Klerk, A. Voidage variation in packed beds at small column to particle diameter ratio. *AIChE J.* **2003**, *49*, 2022-2029.

(12) Aiouache, F.; TSaoir, M.N.; Kitagawa, K. Screening wall effects of a thin fluidized bed by near-infrared imaging. *Chem. Eng. J*. **2011**, *167*, 288-296.

(13) Winterberg, W.; Tsotsas, E.; Krischke, A.; Vortmeyer, D.A. Simple and coherent set of coefficients for modelling of heat and mass transport with and without chemical reaction in tubes filled with spheres. *Chem. Eng. Sci*. **2000**, *55*, 967-979.

(14) Gladden, L.; Akpa, B.; Anadon, L.; Heras, J.; Holland, D.; Mantle, M.; Matthews, S.; Mueller, C.; Sains, M.; Sederman, A. Dynamic MR Imaging of single- and two-phase flows. *Chem. Eng. Res. Des.* **2006**, *84*, 272-281.

(15) Theuerkauf, J.; Witt. P.; Schwesig, D. Analysis of particle porosity distribution in fixed beds using the discrete element method. *Powder Technol*. **2006**, 165, 92-99.
(16) Roblee, L.H.S.; Baird, R.M.; Tierney, J.W. Radial porosity variation in packed beds. *AIChE J*. **1985**, *4*, 460-464.
(17) Sederman, A.; Alexander, P.; Gladden, L. Structure of packed beds probed by Magnetic Resonance Imaging, *Powder Technol*. **2001**, *117*, 255-269.
(18) Yang, R. T . Gas separation by adsorption processes; Imperial College Press: UK, 1997.
(19) Tobiś, J.; Vortmeyer, D. The near-wall channelling effect on isothermal constant-pattern adsorption, *Chem. Eng.Sci.* **1988**, *43*, 1363-1369.
(20) Kwapinski, W.; Winterberg, M.; Tsotsas, E. Mewes, D. Modeling of the wall effect in packed bed adsorption. *Chem. Eng.Tech*. **2004**, *27*, 1179-1186.
(21) Romkes, S.; Dautzenberg, F.; Van de Bleek, C.; Calis, H. CFD modelling and experimental validation of particle-to-fluid mass and heat transfer in a packed bed at very low channel to particle diameter ratio. *Chem. Eng. J.* **2003**, *96*, 3-13.
(22) Ahmadi Motlagh, A.H.; Hashemabadi, S.H. CFD based evaluation of heat transfer coefficient from cylindrical particles. *Int. Commun. Heat Mass Transfer*. **2008**, *35*, 674-680.
(23) Mueller, G.E. Radial void fraction distributions in randomly packed fixed beds of uniformly sized spheres in cylindrical containers. *Powder Technol*. **1992**, *72*, 269-275.
(24) Mueller, G.E. Prediction of radial porosity distributions in randomly packed fixed beds of uniformly sized spheres in cylindrical containers. *Chem. Eng. Sci*. **1991**, *46*, 706-708.
(25) Dixon, A. Correlations for wall and particle shape effects on fixed bed bulk voidage. *Can. J. Chem. Eng*. **1988**, *66*, 705-708.
(26) Kozeny, J. Uber kapillare leitung des Wassers im Boden. Sitzungsber. AKAD. Wiss. *Wien*, **1927**, *136*, 271-306.
(27) Carman, P. Fluid flow through granular beds. *Trans. Inst. Chem. Eng*. **1937**, 15, S32-S48.
(28) Ergun, S. Fluid flow through packed columns. *Chem. Eng. Prog*. **1953**, *48*, 89-94.
(29) Happel, J. Viscous flow in multiparticle systems: Slow motion of fluids relative to beds of spherical particles. *AIChE J.* **1958**, *4*, 197-201.
(30) Anderson, K. E. B . Pressure drop in ideal fluidization. *Chem. Eng. Sci*. **1961**, 15, 276-297.
(31) Molerus, O.; Druckverlustgleichung fur die Durchstromung von Kugelschuttungen im laminaren und im Ubergangsbereich. *Chem. Ing. Tech*. **1977**, *49*, 675.
(32) Eisfeld, B.; Schnitzlein, K. The influence of confining walls on the pressure drop in packed beds. *Chem. Eng. Sci*., **2011**, *56*, 4321-4329.
(33) Moise, A.; Tudose, R. Air isothermal flow through packed beds. *Exp. Therm. Fluid. Sci.*, **1998**, *18*, 134-141.
(34) Ding, Y.; Wang, Z.; Wen, D.; Ghadiri, M.; Fan, X.; Park, D. Solids behaviour in a gas-solid two-phase mixture flowing through a packed particle bed. *Chem. Eng. Sci.*, **2005**, *60*, 523-5239.
(35) tSaoir, M.N.; Fernandes, D.L.A.; Sa, J.; Kitagawa, K.; Hardacre, C.; Aiouache, F. Three dimensional water vapour visualization in porous packing by near-infrared diffuse transmittance tomography, *Ind. Eng. Chem. Res.* **2012**, *51*, 8875-8882
(36) tSaoir, M.N.; Fernandes, D.L.A.; McMaster, M.; Kitagawa, K.; Hardacre, C.; Aiouache, F. Transient distributions of composition and temperature in a gas–solid packed bed reactor by near-infrared tomography. *Chem. Eng. J.* **2012**, *189– 190*, 383– 392
(37) Celik, I.B.; Ghia, U.; Roache, P.J.; Freitas, C.J.; Coleman, H,; Raad, P.E. Procedure for estimation and reporting of uncertainty due to discretization in cfd applications. *J. Fluids Eng*. **2008**, *130*, 078001
(38) Delgado, J. M. P. Q. Longitudinal and transverse dispersion in porous media. *Chem. Eng. Res. Des*. **2007**, *85*, 1245-1252
(39) Spedding, P.L.; Spencer, R.M. Simulation of packing density and liquid flow in fixed beds. *Comput. Chem. Eng*. **1995**, *19*, 43-73.

(40) Reyes, S.C.; Iglesia, E. Monte Carlo simulations of structural properties of packed beds. *Chem. Eng.Sci*. **1991**, *46*, 1089-1099.
(41) Nolan, G.T.; Kavanagh, P.E. Computer simulation of random packing of hard spheres. *Powder Technol.* **1992**, *72*, 149-155.
(42) Crider, J.E.; Foss, A.S. Computational studies of transients in packed tubular chemical reactors. *AIChE J*. **1996**, *12*, 514-522.
(43) Nolan, G.T.; Kavanagh, P.E. Octahedral configurations in random close packing. *Powder Technol.* **1995**, *83*, 253-258.
(44) Benenati, R.F.; Brosilow, C.B. Void fraction distribution in beds of spheres. *AIChE J*., **1962**, *8*, 359-361.
(45) Chan, S. K.; Ng, K.M. Geometrical characteristics of the pore space in a random packing of equal spheres. *Powder Technol*. **1988**, *54*, 147-155.
(46) Spedding, P. L .; Spencer, R. M . Simulation of packing density and liquid flow fixed beds-II. Voronoi polyhedra studies. *Comput. Chem. Eng*. **1998**, *22*, 247-257.
(47) Parse, J.; Wert, J. A geometrical description of particle distributions in materials. *Modelling .Simul. Mater. Sci.Eng*. **1993**, *1*, 275-296
(48) Lindquist, W.B.; Lee, S.M.; Cork, D.A.; Jones, K.W.; Spanne, S. Medial axis analysis of void structure in three-dimensional tomographic images of porous media. *J. Geophys. Res.*, **1996**, *101*, 8297-8310.
(49) Zou, R.P.; Yu, A.B. The packing of spheres in a cylindrical container: The thickness effect. *Chem. Eng. Sci*. **1995**, *50*, 1504-1507.
(50) Mueller, G.E. Radial porosity in packed beds of spheres. *Powder Technol*. **2010**, *203*, 626-633.
(51) Delgado, J.M.P.Q. A critical review of dispersion in packed beds. Heat Mass Transfer. 2006, *42*, 279-310
(52) Augier, F. Idoux, F. Delenne, J. Y. Numerical simulations of transfer and transport properties inside packed beds of spherical particles. *Chem. Eng. Sci*. **2010**, *65*, 1055-1064.
(53) Zhavoronkov, N.M. Aerov, M.E.; Umnik, N.N. Hydraulic reisistance and densityof packing of a granular bed. *J. Phys. Chem*., **1949**, *23*, 342-361.
(54) Reichelt, W. Zur Berechnung des Druckverlustes einphasig durchstromter Kugel-und Zylinderschuttungen. *Chem. Ing. Technol*. **1972**, *44*, 1068-1071.
(55) Atmakidis, T.; Kenig, E. Y. CFD-based analysis of the wall effect on the pressure drop in packed beds with moderate tube/particle diameter ratios in the laminar flow regime. *Chem. Eng. J.* **2009**, *155*, 404–410
(56) Augier, F; Laroche, C.; Brehon, E. Application of computational fluid dynamics to fixed bed adsorption calculations: Effect of hydrodynamics at laboratory and industrial scale. *Separation and Purification Technology* **2008**, *63*, 466–474

APPENDIX A1

The number of scattering or optical depth (OD) according to equation (A.1).

$$\frac{I_{exit}}{I_{Inlet}} = e^{-OD} \qquad (A.1)$$

where I_{exit} and I_{inlet} are light intensities at the exit and the inlet of the packed bed.[34] The OD indicates the number of direction changes of the light through the packing. The imaging is, therefore, constructed by a combination of ballistic and snake photons (less than one scattering, OD< 1) and scattered photons (multiple scattering, OD>1) that pass straight, roughly straight, scattered or diffusively through the medium.

APPENDIX A2

The numerical errors of the simulation were assessed by guidelines provided by Celik et al [37] to insure if the results independent of mesh size. First the representative grid size h procedure is defined as:

$$h=\left(\frac{1}{N}\sum_{i=1}^{N}\Delta V_i\right)^{1/3} \qquad (A.2.1)$$

Where Δ V is the cell volume and N is the number of cells. Three grids grid refinement factor higher than 1.3 was used for the ultimate refinements. The apparent order *m* of the method is defined by (A.2.2) to (A.2.4.) equations:

$$m=\left|\ln\left|\Theta_{32}/\Theta_{21}\right|+q(m)\right|/\ln(r_{21}) \qquad (A.2.2)$$

$$q(m)=\ln\left(\frac{r_{21}^{m}-s}{r_{32}^{m}-s}\right) \qquad (A.2.3)$$

$$s=1.\mathrm{sgn}(\Theta_{32}/\Theta_{21}) \qquad (A.2.4)$$

Where $h_1<h_2<h_3$, $r_{21}=h_2/h_1$, $r_{32}=h_3/h_2$, $\Theta_{32}=P_3-P_2$, $\Theta_{21}=P_2-P_1$. $P_k(k=1, 2, 3)$ expresses the pressure values taken at arbitrary three grid locations in the packed bed and sgn is the function signum.
Equation (A.2.3) should be solved numerically for m. This is then used to find the extrapolated value for the pressure equation (A.2.5), the relative error (equation A.2.6) and the fine grid convergence GCI (equation A.2.7)

$$P_{ext}^{21}=\frac{r_{21}^{m}P_1-P_2}{r_{21}^{m}-1} \qquad (A.2.5)$$

$$e_a^{21}=\frac{P_1-P_2}{P_1} \qquad (A.2.6)$$

$$GCI=\frac{1.25e_a^{21}}{r_{21}^{m}-1} \qquad (A.2.7)$$

APPENDIX A3

Among well-established models, Carman [27], Ergun [28], Zhavoronkov et al.[53] and Reichelt [54] are often cited in literature to estimate pressure drops in low AR packed beds. Ergun proposed a semi-empirical correlation (equation (A.3.1)) by linking the Kozeny-Carman equation for the creeping flow regime and the Burke-Plummer equation for the turbulent regime. Ergun's correlation accounts for viscous and inertial energy losses and relates them to the dynamic variable, velocity of the fluid, as well as the structure of the bed, as characterised by the bed average porosity, *ε*. The dimensionless pressure drops, *P*, is expressed by equation (A.3.1).

$$P=\frac{150(1-\varepsilon)^2}{Re_{dp}\varepsilon^3}+1.75\frac{1-\varepsilon}{\varepsilon^3} \qquad (A.3.1)$$

Where $P=\frac{\Delta p}{L}\frac{dp}{\rho u_s}$ (A.3.2)

The above equation holds for the case of large AR (AR>15) where the condition of near uniformity prevails in the porosity throughout the bed.

- Carman model, as shown by equation (A.3.3), predicts well pressure drop at large AR and therefore can be used as reference model to estimate pressure drop deviations at low AR. [53]

$$P = \frac{6^{3-n}k}{Re_{dp}^{2-n'}}\frac{(1-\varepsilon)^{3-n}}{\varepsilon^3} \qquad \text{(A.3.3)}$$

Where n'=1 and k=5.

- Zhavoronkov equations illustrated by equation (A.3.4) [53]

$$P = \frac{165.35A_w}{Re_{dp}}\frac{(1-\varepsilon)^2}{\varepsilon^3} + 1.2B_w\frac{1-\varepsilon}{\varepsilon^3} \qquad \text{(A.3.4)}$$

Where

$$A_w = B_w = 1 + \frac{1}{2\left(\frac{D}{dp}\right)(1-\varepsilon)} \qquad \text{(A.3.5)}$$

- Reichelt model is illustrated by equation (A.3.6)[54]

$$P = \frac{154A_w^2}{Re_{d_p}}\frac{(1-\varepsilon)^2}{\varepsilon^3} + \frac{A_w}{B_w}\frac{1-\varepsilon}{\varepsilon^3} \qquad \text{(A.3.6)}$$

With the wall correction terms

$$A_w = 1 + \frac{2}{3\left(\frac{D}{d_p}\right)(1-\varepsilon)} \qquad \text{(A.3.7)}$$

$$B_w = \left[1.15\left(\frac{d_p}{D}\right)^2 + 0.87\right]^2 \qquad \text{(A.3.8)}$$

Where A_w and B_w are model constants, d_p is particle size and D is the tube diameter.

The last two models of Zhavoronkov and Reichelt are based on extensive experimental data where Ergun's constants are corrected by considering wall effects.

APPENDIX A4

The fluid flow model was computed from a 2D Brinkman-Forchheimer model that accounts for porosity changes along the radial coordinate of the packing.[56]

$$\rho(u.\nabla u) = -\nabla pI + \nabla.\left(\mu(\nabla u + (\nabla u)^T - \frac{2}{3}\mu(\nabla.u)I\right) + F \qquad \text{(A.4.1)}$$

$$\rho\nabla.u = 0$$

The drag force per unit of volume F is expressed using Ergun's relation as:

$$F = \frac{\mu u}{K} - \beta\rho u^2 \qquad (A.4.2)$$

The permeability of the porous media K and the non-Darcy term β are calculated from Zhavoronkov's model.

Tables

Table 1. Setting parameters of DEM based modelling

	Wall parameters	Particle parameters
Normal stiffness coefficient	10^{13}	2.5×10^{8}
Tangential stiffness coefficient	10^{13}	2.5×10^{8}
Friction coefficient	0.2	0.2
Density	-	3900 kg/m^3

Table 2. Porosity trends for AR from 1.5 to 5

Aspect Ratio D/dp	Porosity (ε)	Deviation (%)*
1.5	0.688	4.36
2.0	0.575	0.52
2.5	0.530	1.51
3.0	0.528	2.08
3.5	0.572	5.77
4.0	0.547	2.74
4.5	0.525	5.52
5.0	0.498	5.02

* Porosity data by Zou et al.[49]

Figures

(a_1)

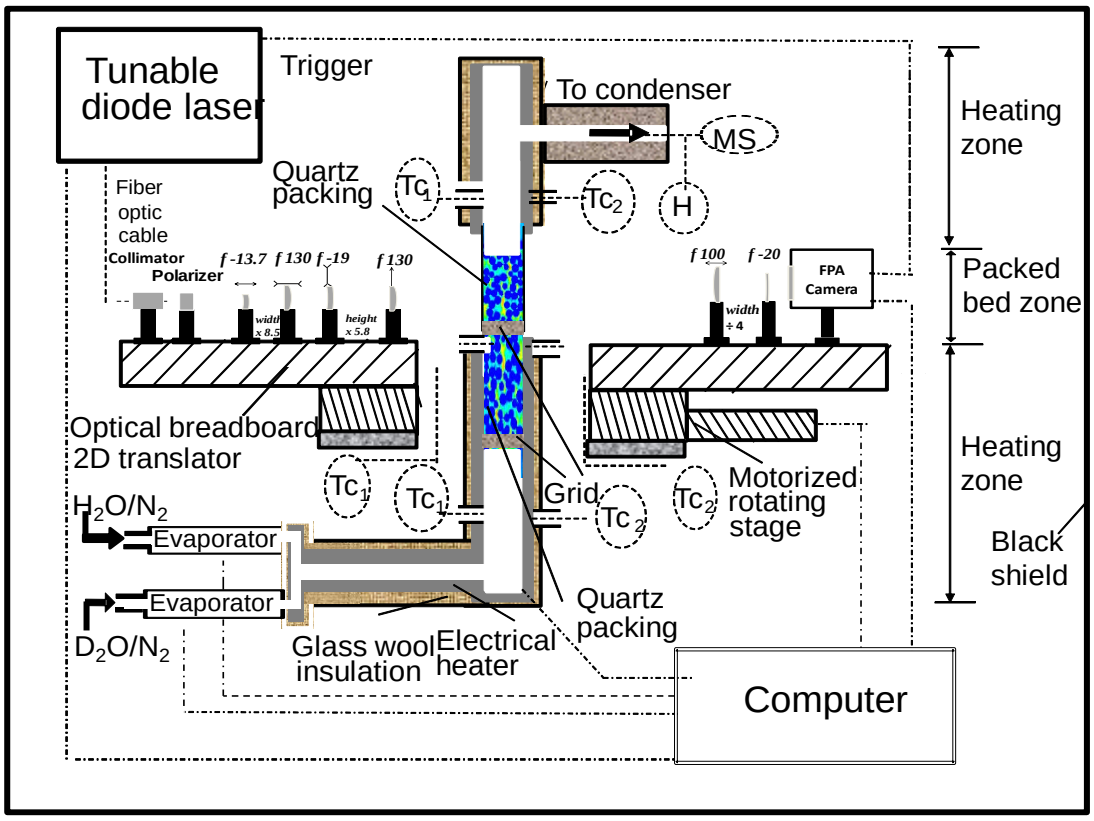

(a_2)

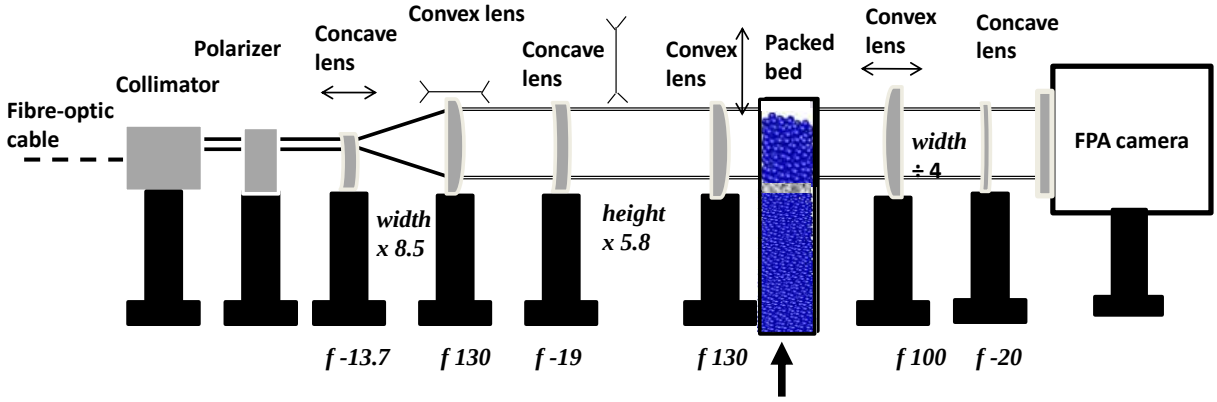

(b) (c)

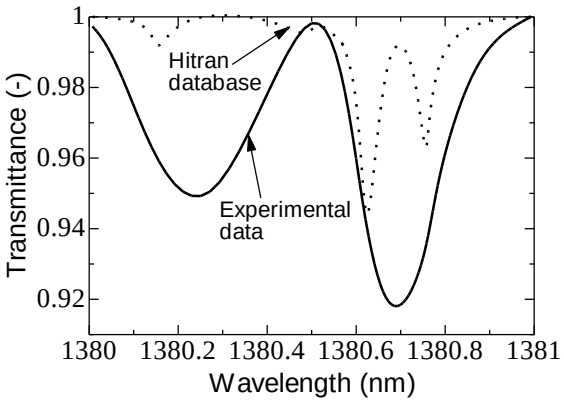

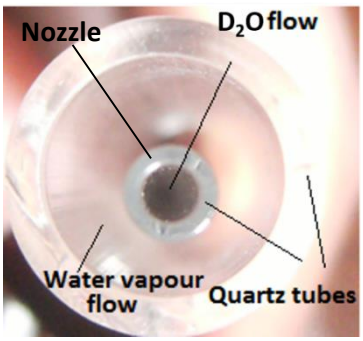

Figure 1. Scheme of the whole tomography apparatus (a_1), optical setup (a_2), spectra of water vapour (b) and Nozzle design top view (c). Nozzle diameter: 5 mm, packed bed tube diameter: 12 mm, thickness of both tubes: 1 mm, Evaporator (Bronkhorst)= Mass flow controller (N_2), air-actuated switching valve, distilled water bath; H: Humidity sensor; TC_1= Thermocouples (monitoring), TC_2: Thermocouples connected to programmable temperature controllers; MS: Mass spectrometer; Optics=details of optics are shown in Figure 1b; Tuneable diode laser: Lock-in monomode connected to FPA camera; pre-packed bed mixer, quartz bead packed bed= Height:39 cm; visible aperture by NIR camera: 1.20 x 5.4 cm^2. Monomode fibre-optic cable connected to a collimator with a top-hat beam shaper (size: 5 mm); polarizer, two couple of cylindrical lenses of focal points *f* (mm)*: f*-13.7, *f*-130 and *f*-19, *f*-130, trans-illuminated backed bed and couple of lens (*f*-100, *f*-20) and intercepted beam size by FPA detector.

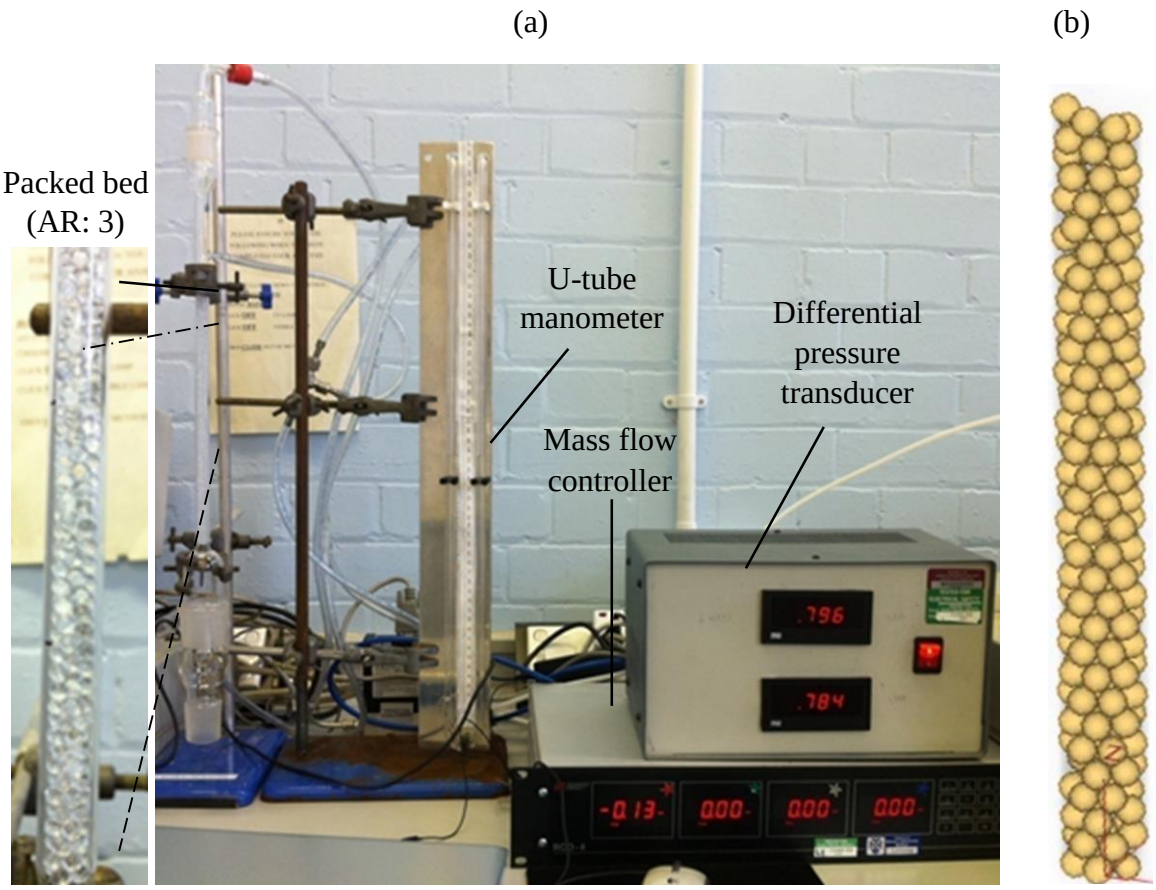

Figure 2. Pressure drops setup (a) and generated packing for AR of 3 by DEM (b)

(a) (b)

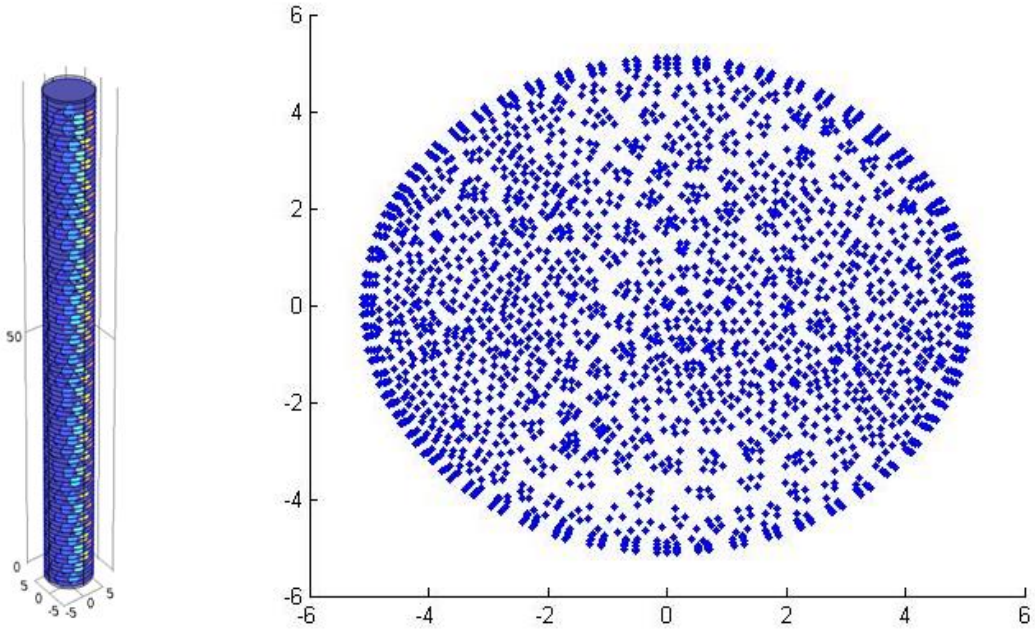

(c)

1. Domain index was allocated integer numbers of "unity" for the between particle domain and "zero" for all solid phase domains

2. The volumetric 3D data were reduced to 2D data by averaging along the angular coordinate: $\varepsilon_s(r,z)=\frac{\int DI(r,\theta,z)\theta d\theta}{\int \theta d\theta}$

3. The 2D surface data were reduced into 1D by averaging along the length (axial coordinate) $\varepsilon(r)=\frac{\int \varepsilon_s(r,z)dz}{dz}$

4. The 1D surface data were reduced into the full porosity of the bed by averaging along the radial coordinate $\varepsilon=\frac{\int \varepsilon(r)dr}{dr}$

Figure 3. Reduction procedure of volumetric 3D domain index data. (a) Cross-sectional slicing of domain index, (b) Irregular distribution of domain index data retrieved and (c) Averaging procedure from 3D domain index to 2D and to 1D data.

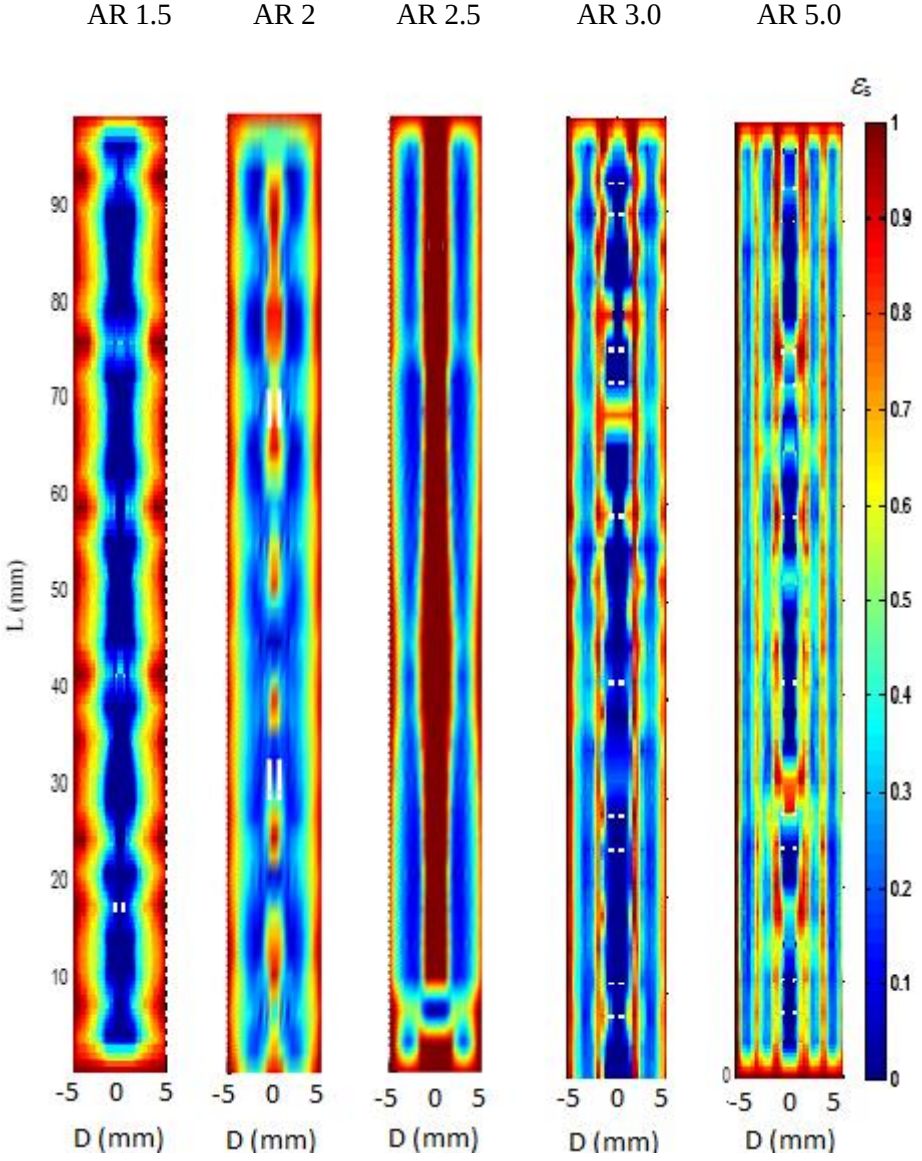

Figure 4. Spatial distribution of surface fraction ε_s of the solid particles for packed beds of ARs from 1.5 to 5

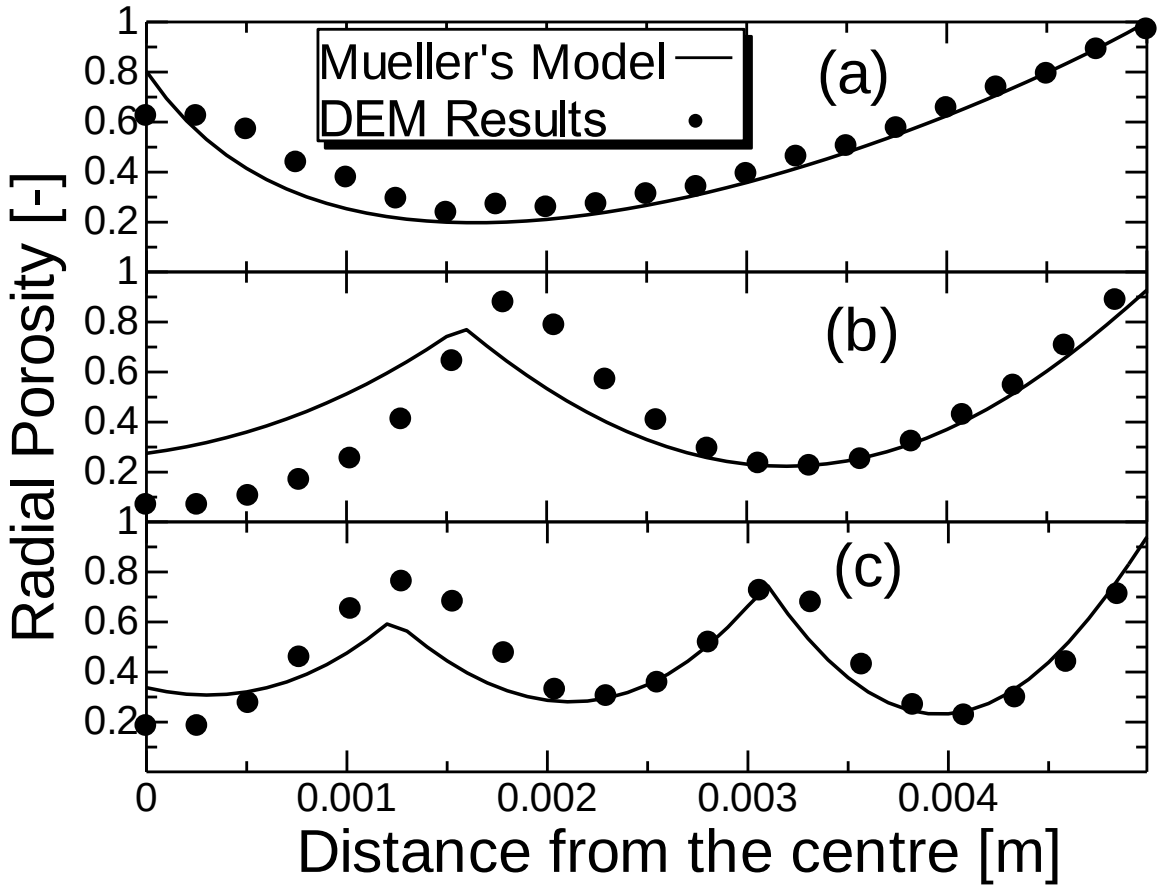

Figure 5. The averaged porosity variation along the radial coordinates at (a) AR: 2, (b) AR: 3 and (c) AR: 5. (Dots: simulation data and lines: Mueller's model [50])

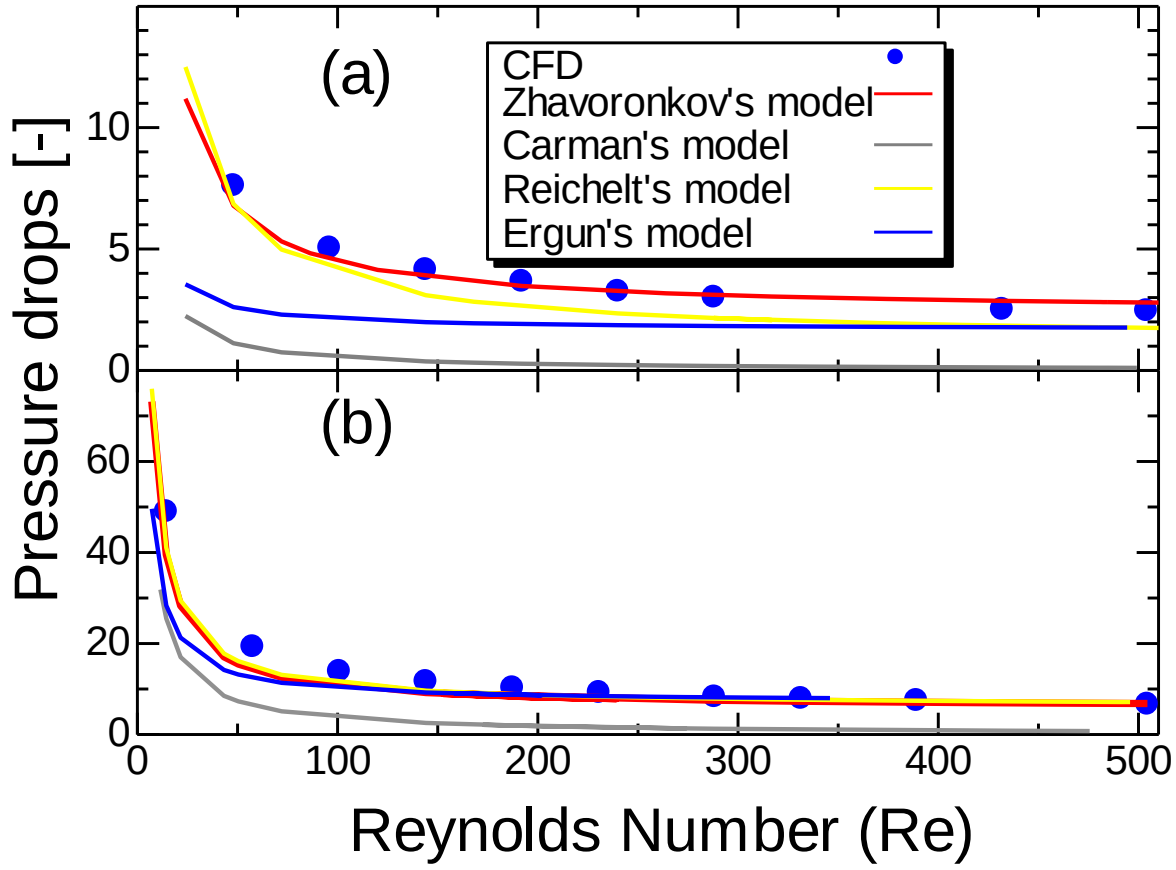

Figure 6. Pressure drop profiles for (a) AR: 1.5 and (b) AR: 5, dot: CFD simulation

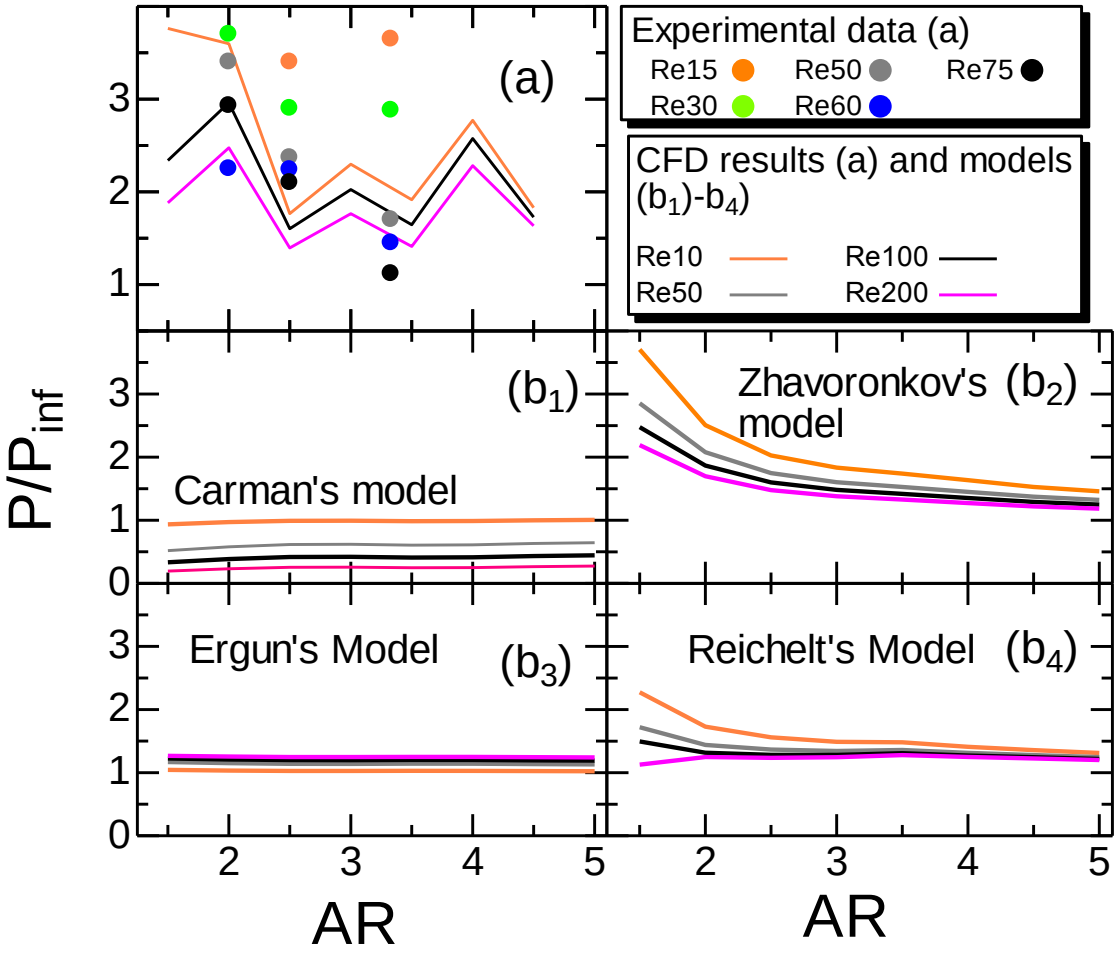

Figure 7. Ratio of pressure drop to pressure drop of infinite packing profiles, (a) simulation, (b) experimental and (b_1-b_4) Carman, Zhavoronkov, Ergun and Reichelt models

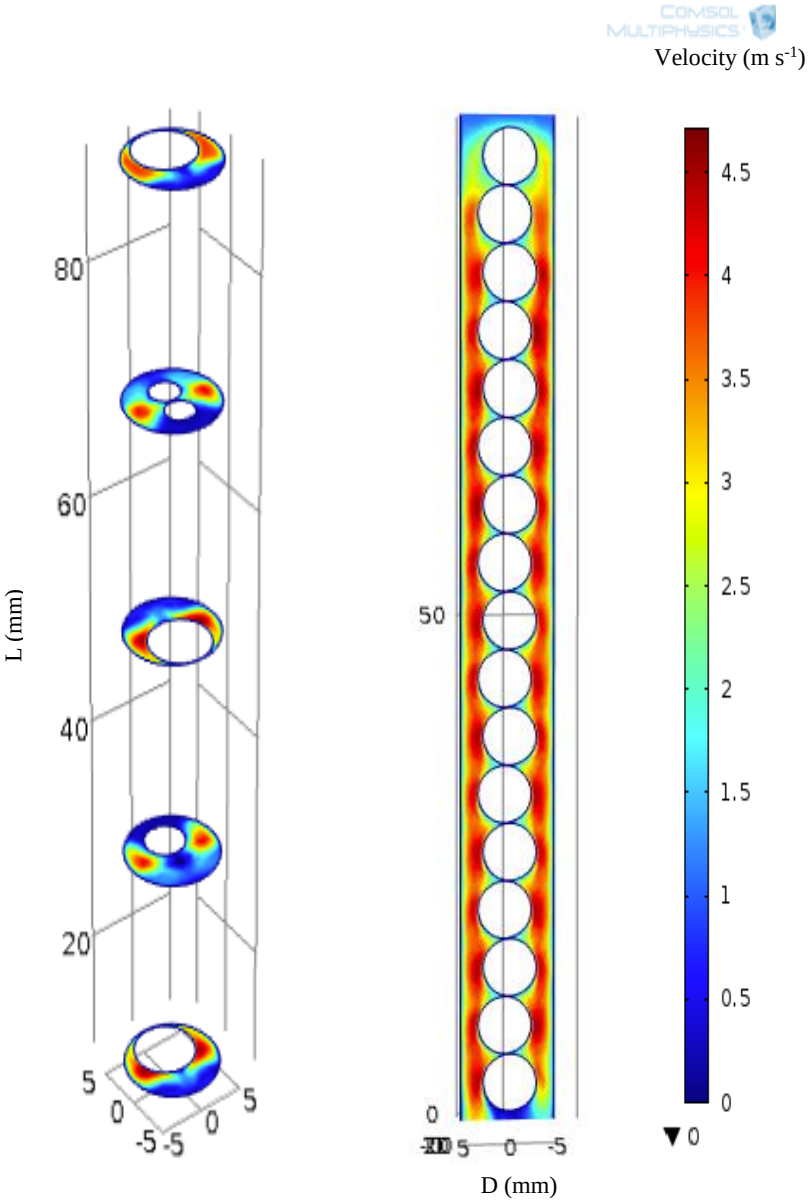

Figure 8. Cross-sectional and vertical cuts of the velocity (m/s) inside a packed bed reactor: AR 1.5 and *Re*= 375

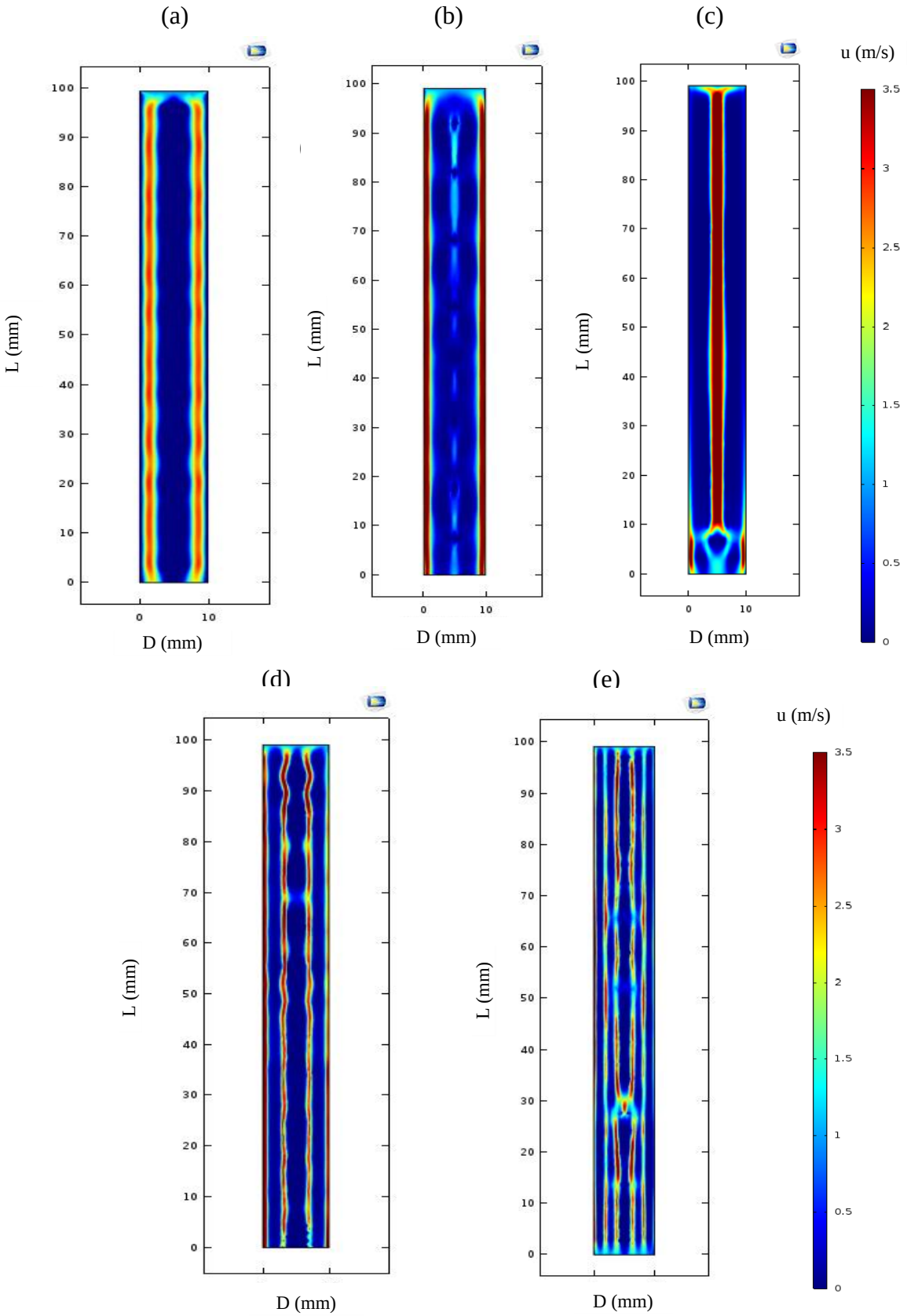

Figure 9. The velocity distribution in 2D profile in a packed bed reactor, (a) AR1.5, (b) AR2, (c) AR 2.5, (d) AR3 and (e) AR5.

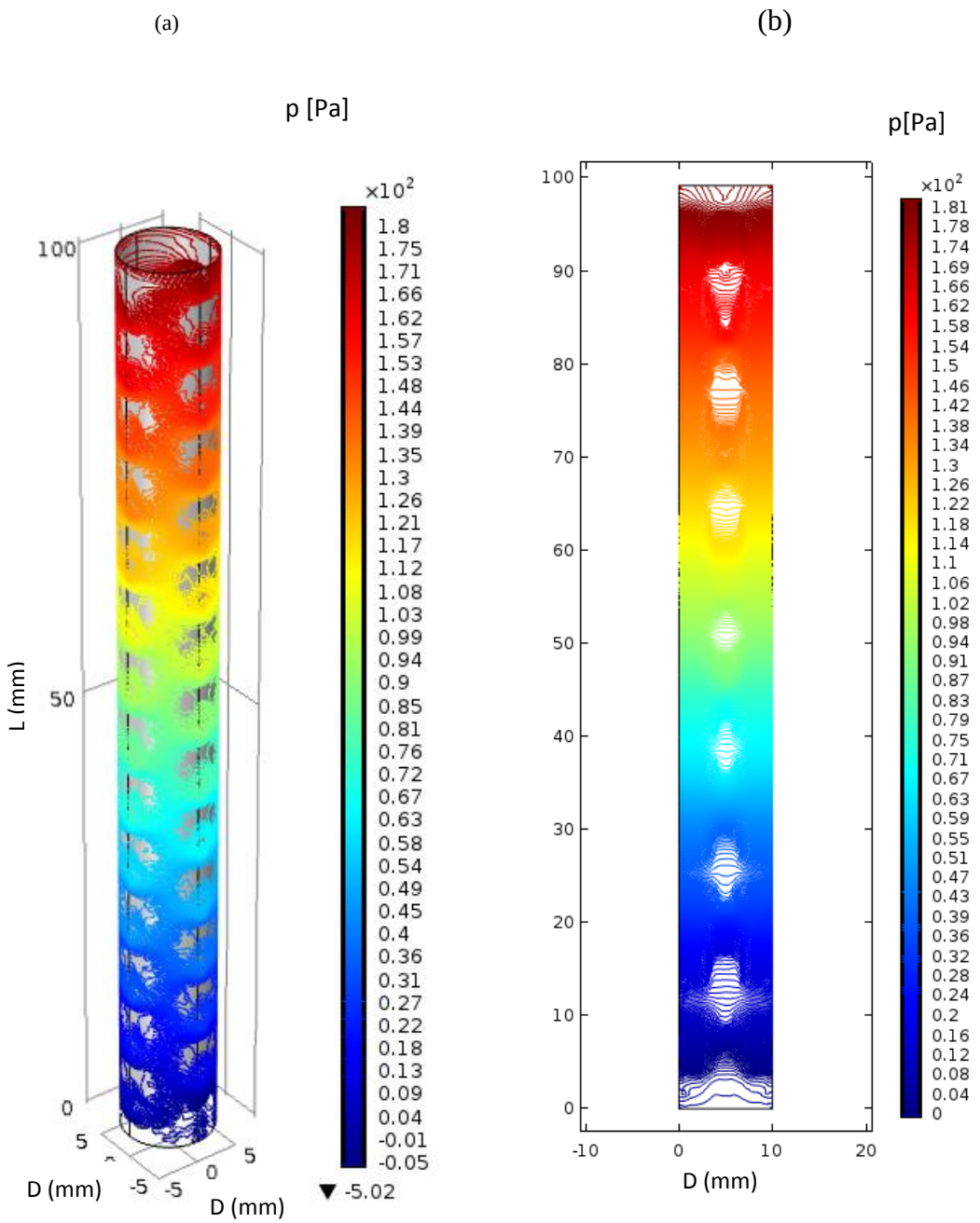

Figure 10. Pressure drop contours for AR: 2 (a) 3D modelling and (b) 2D modelling (*Re*= 284)

(a) (b)

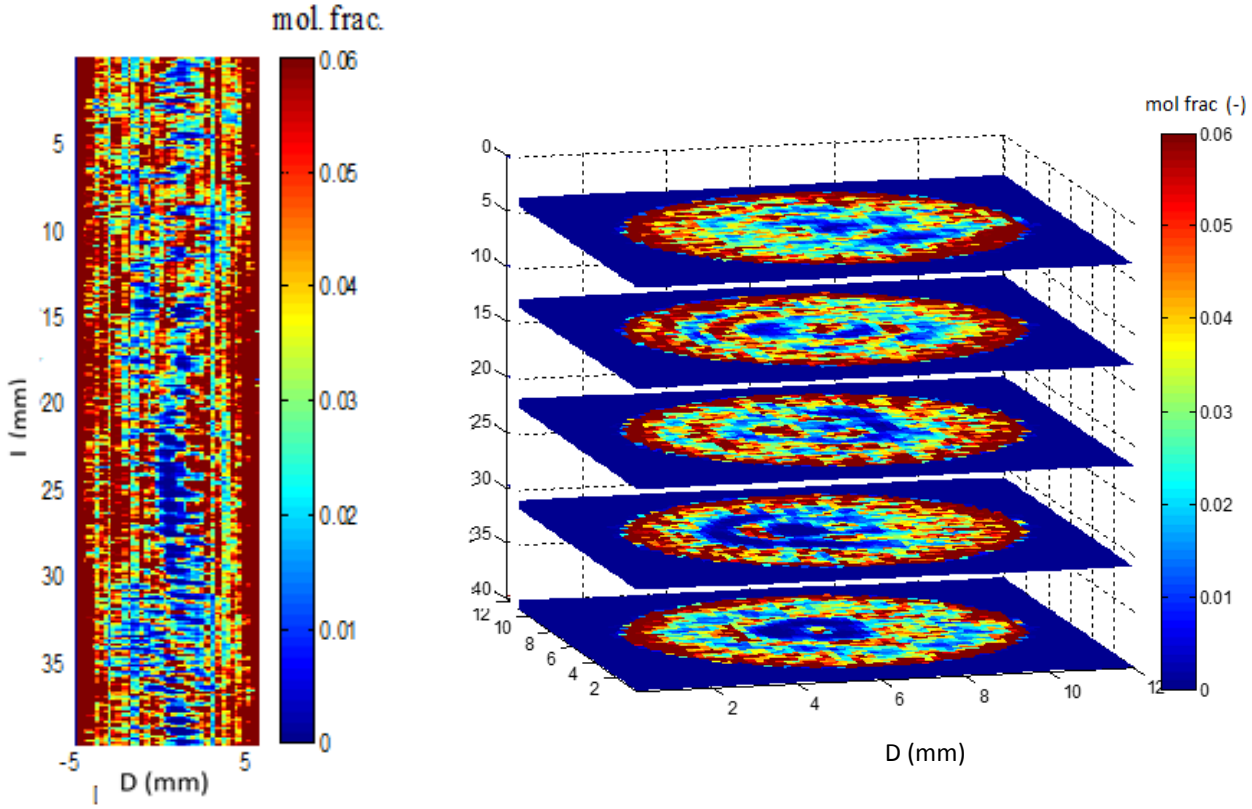

Figure 11. Phantom test by NIR tomography H_2O_v composition maps, (a) vertically sectional maps, (b) five equidistant cross-sectional maps. Inner nozzle diameter: 5 mm, outer tube diameter: 12 mm, thickness of both tubes: 0.5 mm, inlet velocity: 0.1 m s^{-1}.

(a1)

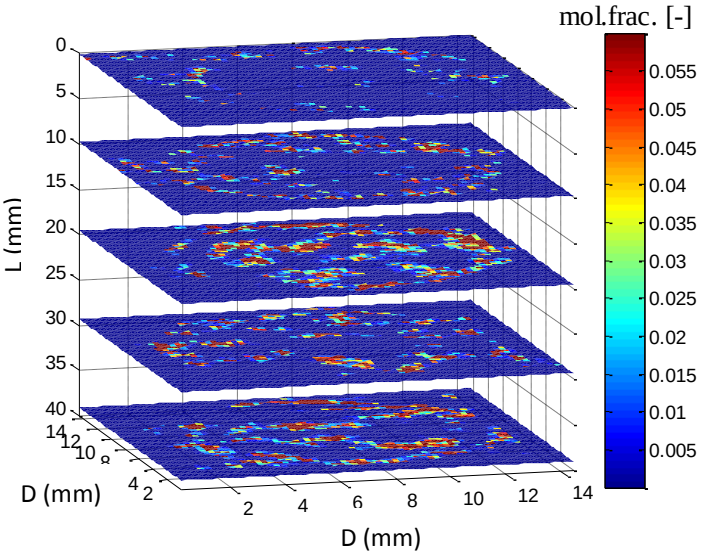
mol.frac. [-]
0.055
0.05
0.045
0.04
0.035
0.03
0.025
0.02
0.015
0.01
0.005
L (mm)
0
5
10
15
20
25
30
35
40
D (mm)
2
4
6
8
10
12
14

(b1)

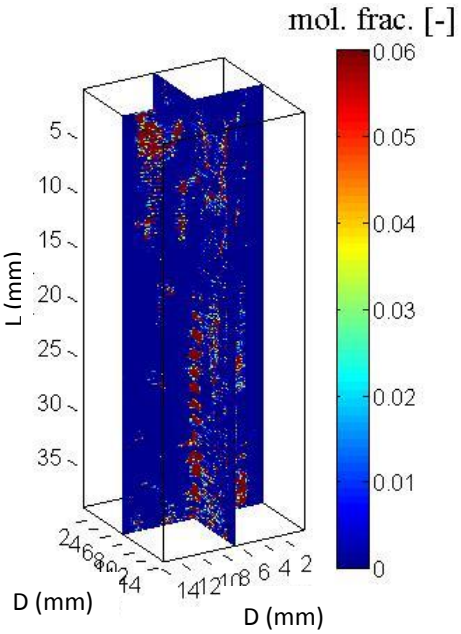
mol. frac. [-]
0.06
0.05
0.04
0.03
0.02
0.01
0
L (mm)
5
10
15
20
25
30
35
D (mm)
D (mm)

(c1)

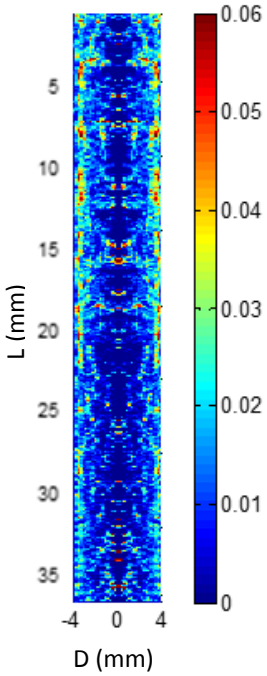
0.06
0.05
0.04
0.03
0.02
0.01
0
L (mm)
5
10
15
20
25
30
35
-4
0
4
D (mm)

(d1)

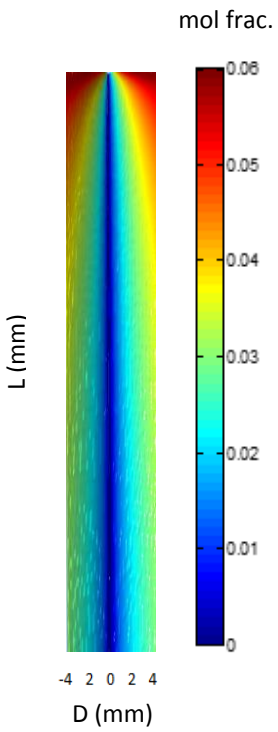
mol frac.
0.06
0.05
0.04
0.03
0.02
0.01
0
L (mm)
-4 2 0 2 4
D (mm)

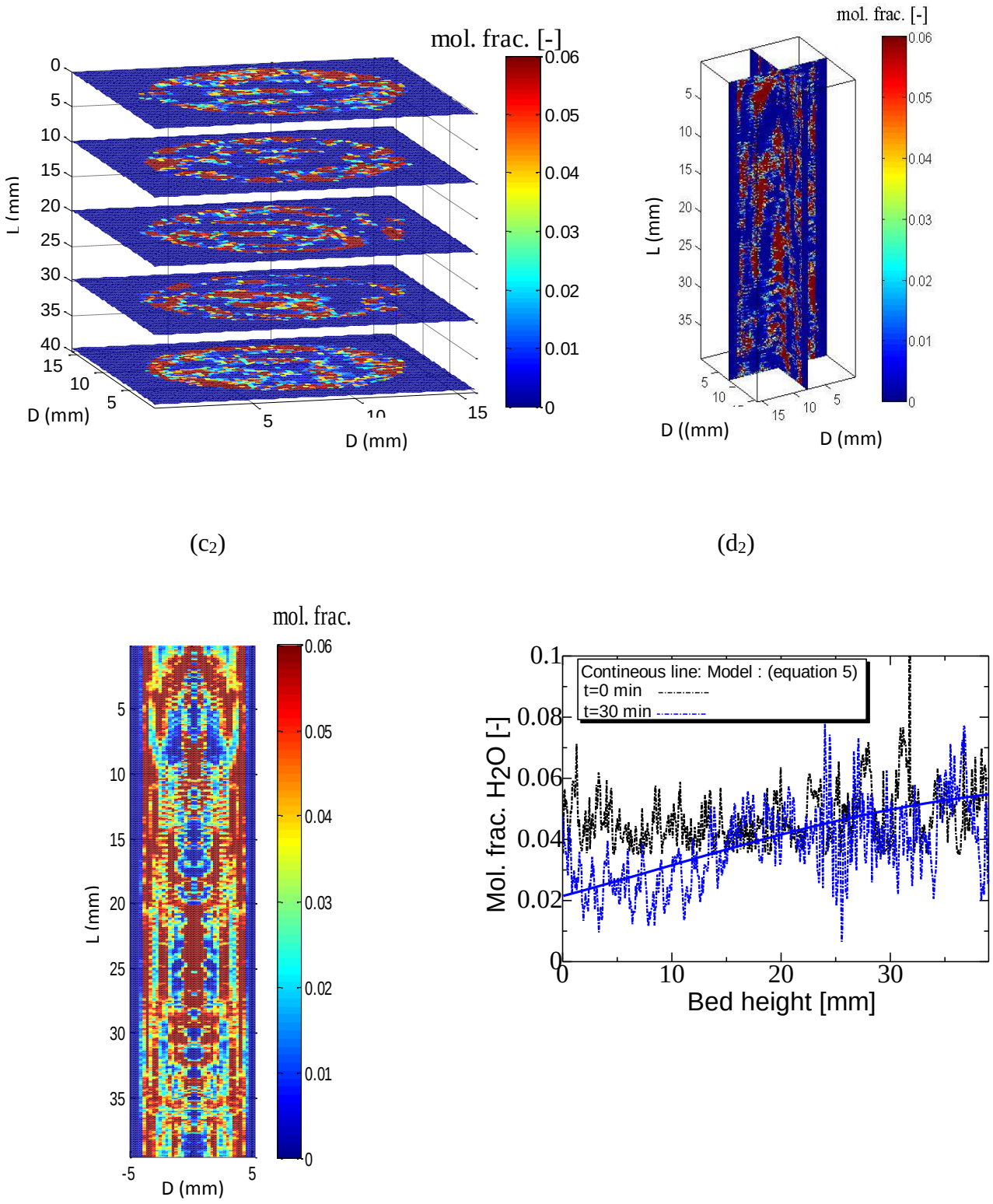

Figure 12. Visualization of H_2O_v composition by NIR imaging, (a_1-d_1) Radial dispersion experiments and (a_2-d_2) axial dispersion experiments. Inner nozzle diameter: 5 mm, quartz tube diameter: 12 mm, thickness of both tubes: 0.5 mm. a_1, a_2: equidistant cross-sectional maps of H_2O_v, b_1, b_2: vertically sectional maps, c_1, c_2 circumferentially averaged maps and d_2: circumferentially and radially averaged maps (straight line model), inlet velocity: 0.00011 m s^{-1}.

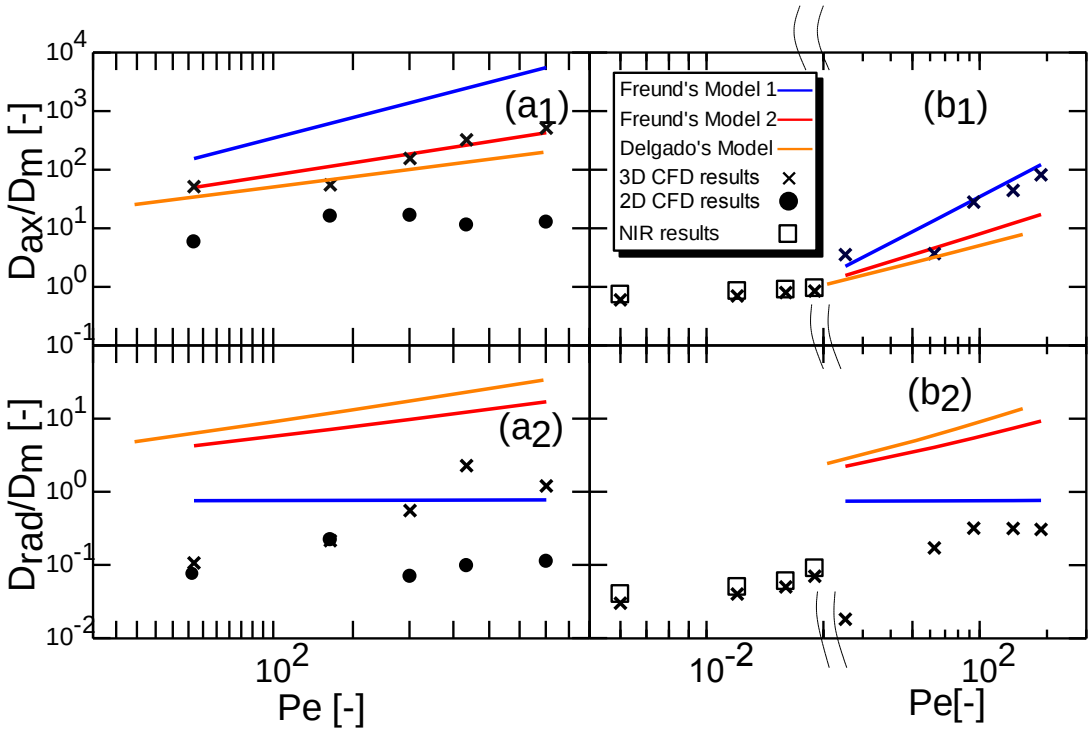

Figure 13. Axial and radial dispersion coefficients along with flow dynamics, respectively: (a_1, a_2) for AR of 2, (b_1, b_2) for AR of 4

(a_1) (a_2) (b_1) (b_2)

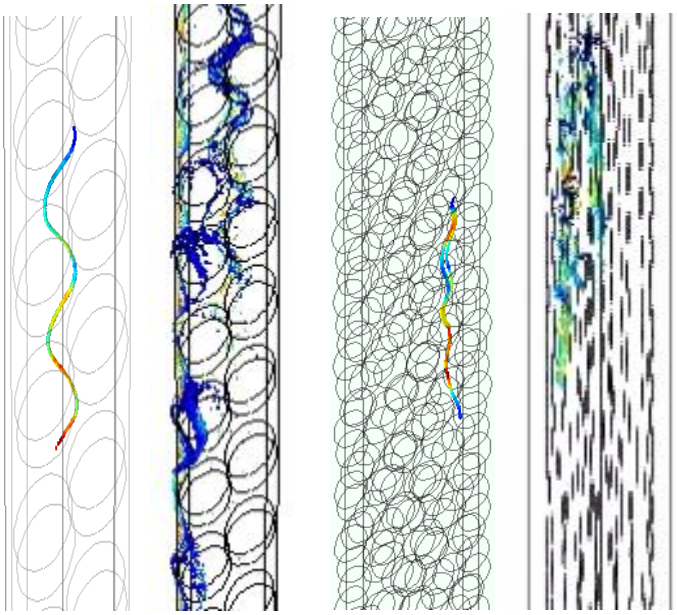

Figure 14 2D vertical slices of particle tracers. AR 2
(a_1: Pe = 0.01 and a_2: Pe=100) and AR 4 (b_1: Pe=0.01 and b_2: Pe=100)